

COMPUTATIONAL DISCOVERY OF TWO-DIMENSIONAL Fe AND Mn COMPOUNDS

A Thesis

Presented to the Faculty of the Graduate School

of Cornell University

In Partial Fulfillment of the Requirements for the Degree of

Master of Science

by

Ziyu Zhou

August 2015

© 2015 Ziyu Zhou

## ABSTRACT

Two-dimensional materials, with their ultimate thinness, maximum surface area, and unique properties, become increasingly attractive for various device applications. We identify several novel iron and manganese two-dimensional compounds using density-functional-theory. Fe and Mn monochalcogenides are stable in an inverted-litharge structure with a low formation energy, which indicates that these materials can be synthesized by, e.g., chemical vapor deposition. Hybrid-density functional calculations predict that MnSe and MnTe are semiconductors, with indirect bandgaps of 2.6 and 2.1 eV, respectively. The band edge positions of both materials straddle the redox potentials of water, showing their potential as photocatalyst for water-splitting. We find that two-dimensional MnSb is magnetic and stable in a square lattice. Using a Heisenberg model we estimate that MnSb is a room temperature ferromagnetic metal. Our prediction can guide new experiment for the synthesis of these new two-dimensional materials for potential applications in energy conversion devices.

## BIOGRAPHICAL SKETCH

Cornell University, College of Engineering, Ithaca, NY

Candidate for Master of Science in Materials Science and Engineering May 2015

University of Science and Technology Beijing, China

Bachelor of Engineering in Materials Science and Engineering, June 2013

I dedicate my dissertation work to my parents for their encouragements from the beginning to the end.

## ACKNOWLEDGMENTS

I wish to express my sincere thanks to Professor Richard G. Hennig, for providing me with all the necessary instructions and generousities in my research. I am also grateful to Professor Paulette Clancy in the Department of Chemical and Biomolecular Engineering, for being the member in my committee and the comments that greatly improved my manuscript. I also show my gratitude to the group members, Houlong Zhuang, Kiran Mathew, Arunim Singh and Ran Duan, for their help and support to my thesis.

Thanks to the impressive computational resources provided by Stampede and Hipergator supercomputer center. I also would like to acknowledge Department of Materials Science and Engineering at Cornell University and the Department of Materials Science and Engineering at University of Florida, giving me the place to conduct all the related computational research on the prediction of different compounds.

## TABLE OF CONTENTS

CHAPTER 1 .....	1
INTRODUCTION .....	1
1.1 Two-Dimensional materials.....	1
1.2 First-principles methods.....	4
1.2.1 Many-body system Schrödinger equation .....	4
1.2.2 Density functional theory.....	5
1.3 Calculation Methods.....	8
CHAPTER 2 .....	11
DISCOVERY OF TWO-DIMENSIONAL Mn and Fe MONO-CHALCOGENIDES AND Pnictides .....	11
2.1 Structure.....	11
2.1.1 Bulk Structure .....	11
2.1.2 Two-dimensional candidate structures .....	13
2.2 Energetic stability .....	14
2.2.1. Convergence .....	14
2.2.2. Energetic stability-formation energy $E_f$ .....	15
2.3. Dynamical stability-phonon spectrum.....	22
2.4 Electronic property.....	24
CHAPTER 3 .....	28
SINGLE-LAYER Mn MONO-CHALCOGENIDE PHOTOCATALYSTS.....	28
3.1 Photocatalytic water splitting.....	28
3.2 Single-layer MnSe and MnTe.....	29
CHAPTER 4 .....	34
MAGNETIC BEHAVIOUR OF TWO-DIMENSIONAL MnSb.....	34
4.1 Introduction.....	34
4.2 Two-dimensional ferromagnet MnSb.....	35
CHAPTER 5 .....	39
CONCLUSION AND FUTURE WORK .....	39
5.1 Conclusion .....	39
5.2 Future work.....	40
APPENDIX.....	46

## LIST OF FIGURES

Fig 1.1 Material tetrahedron (MST)-interrelationship between structures, performance, properties and processing

Fig 1.2 Illustration of DFT approximation

Fig 2.1 Convergence of the total energy with respect to cutoff energy and k-point mesh size for bulk iron sulfide

Fig 2.2 Top and side view of the (i) litharge, (ii) inverted litharge, (iii) distorted-NaCl, (iv) planar hexagonal, and (v) buckled hexagonal structures.

Fig 2.3 Formation energy of all the compounds within the five 2D structure types. The formation energy is defined relative to the energy of the competing bulk structures.

Fig 2.4 Formation energies of synthesized and theoretically predicted 2D materials

Fig 2.5 Formation energies of MX (M = Fe, Mn X = S, Se, Te) MnSb and well-known 2D materials, graphene and MoS<sub>2</sub>

Fig 2.6 Phonon spectra for inverted-litharge MX (M = Fe, Mn X = S, Se, Te) compounds. (a) FeS (b) FeSe (c) FeTe (d) MnS (e) MnSe (f) MnTe

Fig 2.7 PBE band structure calculation for MX (M = Fe, Mn X = S, Se, Te): (a) for FeS (b) for FeSe (c) for FeTe (d) for MnS (e) for MnSe (f) for MnTe

Fig 2.8 HSE06 band structure calculation for MX (M = Fe, Mn X = S, Se, Te): (a) for FeS (b) for FeSe (c) for FeTe (d) for MnS (e) for MnSe (f) for MnTe

Fig 3.1 Illustration of photocatalytic process. Left figure taken from Ref. 5

Fig 3.2 HSE06 band structure for MnSe and MnTe showing that both materials exhibit an indirect band gap.

Fig 3.3 Electrostatic potential at vacuum level to determine the workfunction and electron affinity of MnSe

Fig 3.4 Electrostatic potential at vacuum level to determine the workfunction and electron affinity of MnTe

Fig. 3.5 Band edge positions of single-layer MnSe and MnTe relative to the vacuum level at zero strain show that both 2D materials are potential photocatalysts

Fig 4.1 Structure relaxation of 2D MnSb in the distorted rocksalt structure.

Fig 4.2 Phonon spectrum for two-dimensional MnSb shows that MnSb is stable. The small imaginary modes near the  $\Gamma$  point are likely caused by numerical inaccuracies.

Figure 5.1 The dendrogram of our study

Figure 5.2 illustration of stability of SnO in water

(a) Pourbaix diagram showing the range of stability for the bulk phases Sn, SnO, and SnO<sub>2</sub> (b) Stability of 2D SnO in water against dissolved species

## LIST OF TABLES

Table 1.1 Cohesive energies for bulk solids with BCC, FCC and DIA structures using vdW functionals compared to experimental value.

Table 2.1 Bulk energy of different Fe fraction

Table 2.2 Some two-dimensional materials structures

Table 2.3 Classification of formation energy  $E_f$

Table 2.4 Fundamental indirect and direct band gaps (eV) of single-layer SnS<sub>2</sub> obtained from three different approaches. Experimental optical band gaps are for comparison

Table 3.1 Energy summarization of water splitting

Table 4.1 Magnetic properties of 2D MX compounds

Table 4.2 Estimation of Curie temperature

## LIST OF ABBREVIATIONS

MST: materials tetrahedron  
2D materials: two-dimensional materials  
TMD: transition metal chalcogenides  
CVD: chemical vapor deposition  
MBE: molecular beam epitaxy  
AFM: transmission electron microscope  
TEM: atomic force microscope  
DFT: density functional theory  
GGA: generalized gradient approximation  
LDA: local density approximation  
LSDA: local spin density approximation  
PBE: Perdew-Burke-Ernzerhof  
PW91: Perdew-Wang  
VASP: Vienna ab-initio simulation package  
PAW: projector augmented wave  
HSE06: Heyd-Scuseria-Ernzerhof hybrid functional  
 $\Delta E$ : formation energy  
 $E_{2D}$ : the energy of the two-dimensional materials  
 $E_{\text{bulk}}$ : the energy of any mixture of bulk materials  
FM: ferromagnetic  
AFM: antiferromagnetic  
NM: nonmagnetic  
DFPT: density-functional-perturbation-theory  
 $\chi_m$ : magnetic susceptibility  
NN: nearest-neighbor

## LIST OF SYMBOLS

$H$ : hamiltonian operator

$\Psi$ : wave function

$\nabla^2$ : laplacian operator

eV: electron volt

$\mu_B$ : Bohr magneton

$N$ : number of site

CHAPTER 1  
INTRODUCTION

**1.1 Two-Dimensional materials**

Two-dimensional materials have been intensively studied since free-standing graphene, which is an atomic-thick hexagonal lattice made of carbon atom, was first produced in 2003<sup>[1]</sup>. The realization of the graphene fabrication<sup>[2]</sup> motivates theoretical and experimental investigations into other single-layer materials candidates, such as BN<sup>[3]</sup> or ZnO<sup>[4]</sup>.

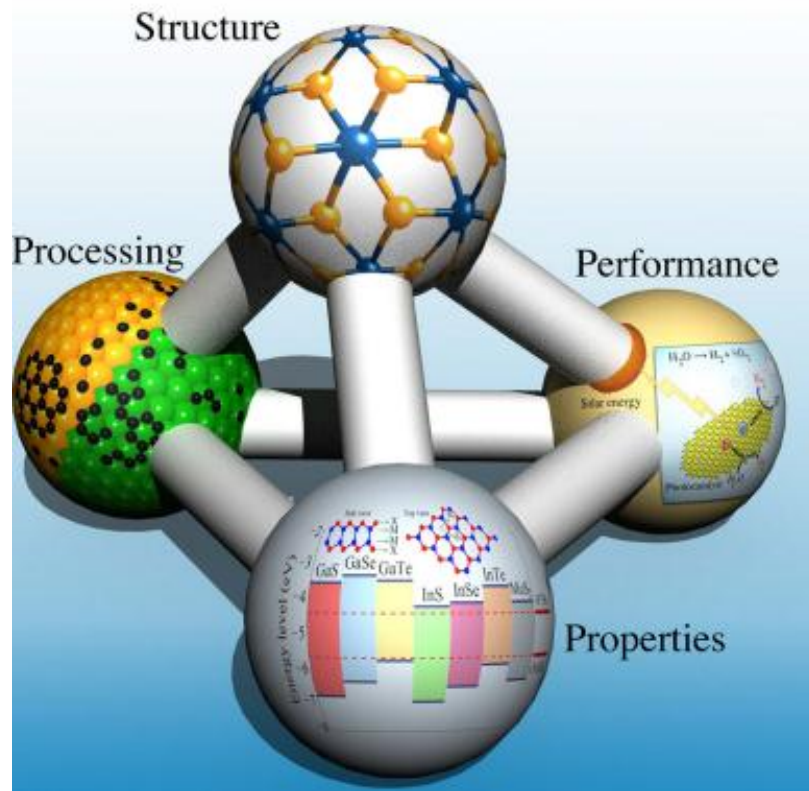


Fig 1.1 Material tetrahedron (MST)-interrelationship between structures, performance, properties and processing (A snapshot is adopted from Ref. 5)

Fig 1.1 shown above is the famous materials tetrahedron (MST)<sup>[5]</sup>. It depicts the four key aspects of materials science – structure, properties, performance, processing – and illustrates their inter-

relationship within the whole materials world, central to the key aspects and their relationship are experimental and theoretical characterization tools.

Two-dimensional materials are materials that are only a few atomic layers thick. Taking a well-known atomically thin material as an example, molybdenum disulfide ( $\text{MoS}_2$ )<sup>[6]</sup>, which is a direct gap semiconductor, it has three sub-layers. The molybdenum atom stays in the middle, sandwiched by top and bottom sulfur atom layers.

In this thesis, we are trying to identify novel 2D materials that are both energetically and dynamically stable. The reduced dimensionality in the z-axis direction and the changes in symmetry make the 2D materials, their properties, such as some novel electronic, optical and magnetic properties, quite different from their bulk counterpart. Among the various properties, the electronic and optical properties are particular attractive for applications as functional materials. Of particular importance are the band-gap for semiconductor applications and the band-alignment and the optical absorption for the photocatalysis. The bandgap of some of the single layer materials lay within the range of visible light, which is beneficial for energy-conversion applications. For instance, single-layer  $\text{CrS}_2$ , with a direct fundamental gap of 1.75 eV, and an optical bandgap of 1.30 eV<sup>[7]</sup>. Subsequently, other layered candidate materials, such as transition metal chalcogenides (TMDs)<sup>[8]</sup> and oxides attract more and more attention. They have a wide range of electronic properties, varying from semiconducting to metallic, even some insulating. Some other interesting properties of 2D materials have been found in the area of superconductivity<sup>[9]</sup> and photocatalysis<sup>[10]</sup>. For example, single-layer  $\text{SnS}_2$  is a photocatalyst with excellent visible-light conversion efficiency shows an incident-photon-to-current-efficiency of 38.7% which is much higher than the existed materials<sup>[11]</sup>. More detailed structure information of these two huge families will be discussed in our following chapters.

Displaying interesting properties and exhibiting the ultimate scale of surface area, two-dimensional materials are ideal for various applications related to catalysis, magnetic, electronic and optical devices. For the past few years, a variety of experimental methods have been developed to synthesize single-layer materials<sup>[12]</sup>. Typical synthesis methods include exfoliation: liquid or mechanical, chemical vapor deposition (CVD) and molecular beam epitaxy (MBE)<sup>[13]</sup>. Some of the 2D materials are exfoliated from their bulk counterparts, such as boron nitride and free-standing graphene. Exfoliation takes advantage of the fact that many bulk parent structures of 2D materials compounds show a layered structure, which is discussed in more details in the following parts. Other 2D materials are synthesized by CVD and MBE, for example the superconducting single-layer FeSe on SrTiO<sub>3</sub><sup>[9]</sup>. The CVD method has been widely used to get large-scale single-layer materials, even with high density of defects, while MBE is an alternative method to synthesis a higher quality atomic scale films<sup>[14]</sup>.

Central to the materials science tetrahedron are characterization techniques, which involve the use of experimental and theoretical tools to analyze the other four key aspects of materials. Common methods includes atomic force microscope (AFM)<sup>[15]</sup>, to determine the thickness of a two-dimensional materials, scanning transmission electron microscope (STEM) to study the structure and some defects, such as grain boundaries in the 2D materials<sup>[16]</sup>. In our study we are trying to use density-functional theory to characterize the properties of two-dimensional materials.

One of the properties that have not received as much attention as others for 2D materials is magnetism. The recent study of monolayer GaSe, illustrates that the introducing of vacancy and chemical element doping could induce net magnetic moment in the single-layer GaSe<sup>[17]</sup>. The study by A. Singh and R. Hennig systematically investigates the group-III and IV mono-chalcogenides<sup>[18]</sup>. It shows that most of the single-layer group III-IV compounds are stable in either litharge structure or distort rock-salt structure, with low formation energy comparable to two-dimensional MoS<sub>2</sub>. Some of

them are suitable for the optoelectronics and solar energy conversion devices, while others are competitive candidates for the water splitting photocatalyst<sup>[18]</sup>. There are also some other researches on transition metal oxides and dichalcogenides. However, no studies have been performed of transition metal monochalcogenides, containing iron and manganese, which could result in magnetism. The theoretical prediction of the two-dimensional structure of iron and manganese monochalcogenides and their properties, is a first step toward the realization of potentially magnetic 2D materials and could pave the way for their synthesis or exfoliation from the bulk materials.

In this thesis, we present a study of single-layer transition metal mono-chalcogenides MX (M = Mn, Fe X= S, Se, Te). We identified their lowest energy within 200 meV/atom of the bulk structures using five candidate structures. We calculated their phonon spectra to ensure the dynamic stability. To investigate the exciting properties for the electronic devices, the generalized gradient approximation PBE and HSE06 hybrid functional band structure calculation and band alignments are conducted to see if these single-layer materials would be useful for the electronic devices or solar energy conversion applications. To further explore the properties of two-dimensional materials, we determine the magnetic properties of single-layer MnSb, using the Heisenberg model to estimate the Curie temperature.

## ***1.2 First-principles methods***

In this chapter, we review the fundamental concepts of density-functional theory, which provides the theoretical foundation for our computational study of two-dimensional materials. For more details we refer the reader to the references<sup>[19,20]</sup>.

### **1.2.1 Many-body system Schrödinger equation**

The Schrödinger equation is a partial differential equation in quantum mechanics and provides the foundation for modern physics, chemistry, and materials science. Basically, by solving the equation

if we could, we would acquire the wave function information and ground-state properties of any system. In its time-independent form it is given by the eigenvalue equation,

$$E\psi = H\psi, \quad (1)$$

where  $E$  is the eigenvalue,  $H$  is the Hamiltonian operator, and  $\Psi$  is the wave function. The Hamiltonian operator includes the kinetics and potential energies terms. In general, many particles included in a crystal solid, we have to consider the interaction between different particles, so it is very difficult to solve the equation. In this part, we briefly introduce the components of the many-electron Hamiltonian operator.

$$H = H_e + H_n \quad (2)$$

$$H_e = -\frac{\hbar^2}{2m} \sum_i \nabla_i^2 + \frac{1}{2} \sum_{\substack{i,j \\ i \neq j}} \frac{e^2}{|r_i - r_j|} - \sum_{I,i} \frac{Z_I e^2}{|r_i - R_I|} + \frac{1}{2} \sum_{\substack{I,J \\ I \neq J}} \frac{Z_I Z_J e^2}{|R_I - R_J|} \quad (3)$$

$$H_n = -\frac{\hbar^2}{2M_I} \sum_I \nabla_I^2 \quad (4)$$

where the  $\nabla_i^2$  and  $\nabla_I^2$  are the Laplacian operators for the particles at different positions. The Hamiltonian operator describes the energy of a many-electron system, where  $m$  is the mass of the electron,  $-e$  the charge and  $r_i$  the position of the  $i$ -th electron.

The problem is that the many body Hamiltonian  $3N$  parameters and is too complicated to solve. In order to simply the problem, approximations need to be made such as, Hartree-Fock-approximation or density-functional-theory.

### 1.2.2 Density functional theory

Density functional theory (DFT) is a method that maps the quantum mechanical many-electron problem onto a single-electron problem. The Hohenberg – Kohn theorem of DFT shows that in principle all properties of a material are determined by the ground-state electron density. The Kohn-Sham formulation of DFT provides a practical method that determines the ground state energy of a many-

electron system using the ground state density. The main variable factor in this theory is the – density, principle electron density. The main approximation in DFT is for the unknown exchange-correlation functional. In this work, we employ DFT to calculate energy differences between different structures and estimate materials’ properties. In the following we outline some of the aspects of DFT, starting with the Hohenberg - Kohn Theorem and Kohn - Sham theory, and finishing with a brief overview of approximations to the exchange-correlation functional.

There are two main parts of the Hohenberg - Kohn Theorem. The first is that the ground-state energy of a many-body system is a functional of the density, specifically electron density, with  $\rho(\vec{r})$  the density of electron,  $E_{\text{system}}$  the energy of the system. In other words, a one-to-one correlation exists between the electron density and system energy. However the actual wavefunction is not described in this theorem.

$$E_{\text{system}} = E[\rho(\vec{r})] \quad (5)$$

The second aspect of the Hohenberg – Kohn theorem is that by minimizing the functional, the ground state energy could be derived. That is  $E_0 = \min [E_{\text{system}}]$ . Owing to this theorem, we could effectively map the complex many-body wave function onto a simpler density related formula. The Kohn - Sham theory provides a practical approach to obtain the unknown energy functional of the Hohenberg-Kohn theorem. The resulting Kohn - Sham equations transform the Hamiltonian operator to a single-electron or Kohn - Sham Hamiltonian operator:

$$\mathcal{H} = T_{\text{KS}}[\rho] + V_{\text{ext}}[\rho] + V_H[\rho] + V_{xc}[\rho] \quad (6)$$

The first term is the KS kinetic energy, which is given by the kinetic energy of a non-interacting electron system. The second term is the external potential of the whole system, and the third part is the Hartree or electrostatic energy. The last term  $V_{xc}[\rho] = \frac{\delta E_{xc}[\rho]}{\delta \rho(r)}$  is called the exchange-correlation potential, the only unknown term in the operator. Figure 1.2 illustrates the mapping onto the non-interacting

electron system of the DFT. The DFT approximation maps the many-electron problem onto a set of effective single-electron problems, simplifying the problem from a  $3N$  dimensional space to a three-dimensional space.

As we mentioned above, there is only one unknown term in the Kohn-Sham Hamiltonian operator, the exchange-correlation potential. Many studies over more than 30 years have investigated various approximations and exact conditions for the exchange-correlation term of DFT. There are several practical approximations that provide accurate energies or properties of materials. The earliest promising approximation was the local electron density approximation, which determines the exchange-correlation potential from the uniform electron gas. It is called *local density approximation* (LDA) <sup>[21]</sup>. However, electron densities in materials deviate from a uniform density, resulting in errors in this approximation. So additional information about the non-uniformity of gradients in the electron density have been investigated and found in many cases to improve the accuracy of DFT. A next approximation containing additional information about electron density beyond the local value of the density is the *generalized gradient approximation* (GGA). Two widely used functionals of the generalized gradient approximation are the Perdew-Wang (PW91) <sup>[22-23]</sup> and the Perdew-Burke-Ernzerhof (PBE) <sup>[24-25]</sup> functionals. Generally speaking, since GGA contains more information, it is often more accurate than LDA, however this is not always the case. Other approximations that include additional information about the curvature of the local density are the meta-GGA and hyper-GGA, which are briefly discussed in the appendix.

A well-known limitation of the local and semi-local approximations to the exchange-correlation potential of DFT, e.g. the LDA and GGA approximations, is the underestimation of the band gap value of semiconductor. Another limitation is the lack of a description of weak van der Waals interactions between atoms and between layers in some compounds. Both the band gap underestimation and the lack

of van der Waals interactions can be overcome by use of functionals that are specifically designed to overcome these shortcomings of semi-local functionals. In our study, we apply the HSE06 hybrid functional for the calculation of the band gap for possible semiconductors and we apply a non-local functional that describes van der Waals interactions to accurately estimate the formation energies of two-dimensional materials relative to their bulk counterpart, which frequently are layered compounds.

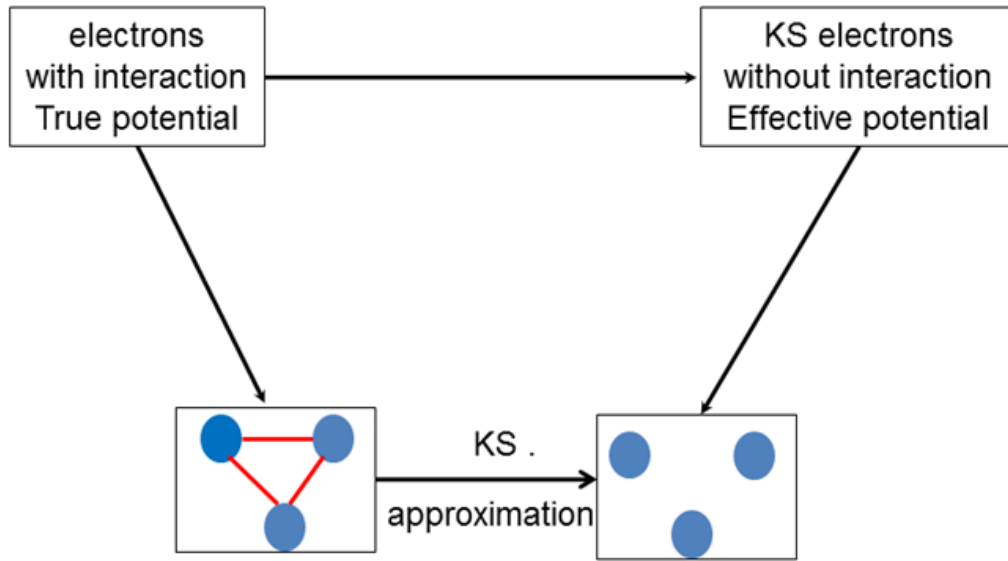


Fig 1.2 Illustration of DFT approximation

### 1.3 Calculation Methods

In this thesis, we apply density functional theory (DFT) calculations using the projector augmented wave (PAW) method implemented in the plane-wave code VASP<sup>[26-29]</sup>. The structural relaxation, formation energy calculations, and phonon calculations, employ the vdW-DF-optB88 functional that includes van der Waals interactions<sup>[30-33]</sup>. There are also other exchange functionals for the van der Waals calculations that could have been chosen here, or more approximate empirical approaches used.<sup>[57]</sup> In order to make a more systematic investigation, it would be worthwhile in the future to compare these other functionals to vdW-DF-optB88. Due to the limited amount of accurate

experimental data available for binding energies of layered systems, we do not attempt such a comparison here, instead we compare to cohesive energies of some 3D bulk structures. We determine the required kinetic energy cut-off and the Brillouin-zone (BZ) sampling for the calculations by converging the total energy to 5 meV/atom. The cut-off energy is 500 eV and a  $35 \times 35 \times 35$  k-point mesh is used for all bulk calculations. We relax all structures until the forces acted on the atoms are below 5 meV/Å. In order to ensure that interlayer interactions for the single-layer structures are negligible, a large vacuum spacing of 18 Å is used. For the band structure calculations, we employ the computationally more demanding Heyd-Scuseria-Ernzerhof (HSE06) hybrid functional<sup>[34]</sup>. Optical absorption of two-dimensional materials is dominated by excitonic states, which are well described by the Bethe-Salpeter equation (BSE), implemented in the VASP code. Due to the very high cost of performing BSE calculations, this remains for future work.

Here, we provide a short discussion about the assessment of our employed methods. Properly applying van der Waals interactions in the theoretical prediction is an important part of the DFT calculation for layered materials. Due to the fact that we are trying to make a successful prediction of some novel 2D materials, we give an example on cohesive energies (in eV/atom) for nine bulk solids with BCC, FCC and Diamond structure to check the validity of employing vdW-DF exchange-correlation functionals shown in a previous work<sup>[54]</sup>. All the experimental cohesive energies<sup>[55]</sup> were corrected by the zero-point vibration energy  $E_{ZPV}$  calculated using the Debye temperature<sup>[56]</sup>. For the cohesive energies, the three chosen vdW functionals show a similar variation, and better results than PAW-GGA, compared to the experimental results, while the optB86b functional shows the least accurate one among the three. This fact provides information on the validity of using vdW-DF functionals.

Table 1.1 Cohesive energies for bulk solids with BCC, FCC and DIA structures using vdW functionals compared to experimental value.

Solid	Crystal structure	optB86b vdW	optB88 vdW	optPBE vdW	PAW GGA	Expt
Li	BCC	1.640	1.586	1.622	1.605	1.663
Na	BCC	1.130	1.070	1.115	1.088	1.128
K	BCC	0.935	0.890	0.926	0.869	0.943
Al	FCC	3.643	3.379	3.339	3.544	3.431
Ni	FCC	5.324	4.978	4.691	4.797	4.484
Cu	FCC	3.755	3.572	3.399	3.485	3.523
C	Diamond	8.034	7.891	7.732	7.851	7.586
Si	Diamond	4.878	4.744	4.656	4.614	4.693
Ge	Diamond	4.018	3.921	3.787	3.742	3.881

## CHAPTER 2

### DISCOVERY OF TWO-DIMENSIONAL Mn and Fe MONO-CHALCOGENIDES AND Pnictides

#### 2.1 Structure

##### 2.1.1 Bulk Structure

We define the chemical compounds MX (M = Fe, Mn; X=N, P, As, Sb, O, S, Se, Te) as the Mn and Fe mono-chalcogenides and pnictides. The MX compounds exhibit a range of bulk crystal structures with different space groups. The bulk MX with M = Fe, Mn and X = P, As occurs in an orthorhombic structure with space group  $Pnma$ . The bulk compounds FeX with X =S, Se, Te crystallize in a layered inverted-litharge structure with tetragonal space group  $P4/nmm$ , where the chalcogen atoms are tetrahedrally coordinated with neighboring Fe atoms. The MnX bulk compounds with X= N, O, S, Te occur in the rock salt structure with the cubic space group  $Fm\bar{3}m$ . Bulk MnSe and FeN occur in a cubic structure with space group  $F\bar{4}3m$ . Bulk FeSb and MnSb crystallize in a hexagonal structure with space group  $P6_3/mmc$ , and FeO occurs in a tetragonal structure with space group  $I4/mmm$  <sup>[35]</sup>.

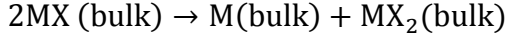
The thermodynamic stability of a phase is given by its free energies. At low temperatures, (T ~ 0 K) the ground state energy provides a good approximation of the free energy and allows us to estimate the phase stability and phase diagram To find the ground state structure of a compound, we have to identify the structure that has a lower energy than any other structures or mixtures. The minimization of the energy of phases with various structures can be visualized by convex hull of the energy, which is obtained from a plot of the formation energies of various structures versus their compositions. All the structures with energies above the convex hull are thermodynamically metastable or unstable against transformation into the lower energy structures represented by points on the convex hull.

In some cases, a thermodynamic stable bulk compound with the same element composition as the single-layer material may not exist. In that case, the reference bulk energy is given by the energy of a mixture of the competing phases with the same composition as the 2D material <sup>[36]</sup>. For example, for some of the 2D MX compounds, no bulk MX phase exists. In that case the energetic stability of the binary 2D MX compound is given relative to the mixture of two competing bulk phases. For example, we follow the reaction below,



Here we take bulk FeSb as an example. It decomposes into bulk Fe, which crystallizes in the bcc structure and bulk FeSb<sub>2</sub>, which occurs in an orthorhombic structure, with space groups  $Im\bar{3}m$  and  $Pnmm$ , respectively:

The energetic stability of these two bulk phases against competing phases is given by the general reaction below



Here we take bulk FeSb as an example; it decomposes into bulk Fe crystallizes in cubic structure and bulk FeSb<sub>2</sub> occurs in orthorhombic structure with the space group  $Im\bar{3}m$  and  $Pnmm$  respectively. To find the energy balance in this reaction, considering the interlayer interaction, we employ vdW-DF-optB88 van der Waals corrections for the exchange-correlation functional. We identify that bulk FeSb is energetically stable by 50 meV/atom

Table 2.1 Bulk energy of different Fe fraction

	Fe	Sb	FeSb <sub>2</sub>
Bulk energy (eV/atom)	-5.64	-2.10	-3.33

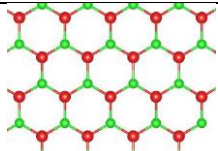
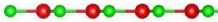
$$E_f(\text{FeSb}_2)\left(\frac{\text{eV}}{\text{atom}}\right) = E(\text{FeSb}_2) - \frac{1}{3}E(\text{Fe}) - \frac{2}{3}E(\text{Sb}) = -50 \text{ meV/atom.}$$

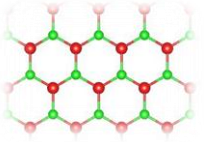
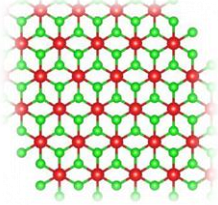
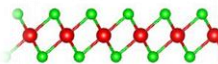
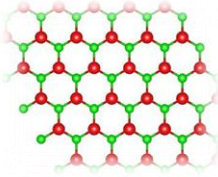
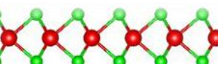
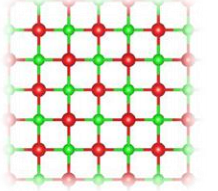
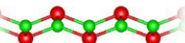
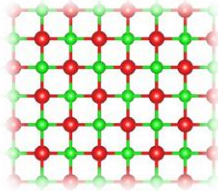
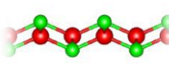
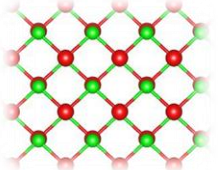
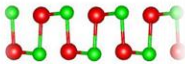
### 2.1.2 Two-dimensional candidate structures

2D materials, with one or few atoms thickness, that can be exfoliated from their bulk counterparts or synthesized by experimental methods, such as CVD and MBE, present a growing family of materials. Various 2D crystal structures were identified in the previous study. Many 2D materials occur in hexagonal structures. In our study we include these hexagonal structure type as well as some common that are not only hexagonal, but exhibit a square lattice. For an overview of several families of layered compounds and corresponding 2D materials, see the work by Valeria Nicolosi *et al* [37].

Table 1.2 summarizes four common hexagonal and three common cubic 2D crystal structures. Hexagonal boron nitride is an atomically thin and perfectly planar, single-layer material. Displace the cations and anions perpendicular to the plane results in the bulked hexagonal structure that was also theoretically proposed for single-component Si. Some of the transition metal dichalcogenides, such as MoS<sub>2</sub>, occur in a structure with three sublayers, where the metal atoms “sandwiched” between two layers of chalcogen atoms. The chalcogen atoms are either in an eclipsing position, in the so-called 2H structure, or shifted relative to each other, in the so-called 1T structure. Reported by Singh *et al* [18], the group-IV monochalcogenides are stable in the 2D litharge structure. In this work, we find all the iron monochalcogenides are stable in a similar structure called inverted-litharge structure, in which the iron atoms occupy the center layer and the chalcogen atoms are located in the top and bottom layers.

Table 2.2 some two-dimensional materials structures

Bravais Lattice	Structure	Top view	Side view	Example
Hexagonal	Planar hexagonal			BN

	Buckled hexagonal			Si
	3-sublayers-1T			MoS <sub>2</sub>
	3-sublayers-2H			MoS <sub>2</sub>
Square	Litharge			PbO
	Inverted-litharge			FeX X=S,Se,Te
	Distorted-NaCl			SnSe

## 2.2 Energetic stability

### 2.2.1. Convergence

Some empirical evidence for DFT calculations and common lore for DFT have shown that the precision of DFT calculations for physical properties is correlated with the precision of the calculation of the total energy. Therefore, we converge the computational parameters of the DFT calculations using the total energy as a benchmark <sup>[38]</sup>. For each of the numerical approximation, we can improve the

precision and converge towards the exact solution for the DFT Hamiltonian by using more and more computational resources. Before performing the DFT calculations for a series of materials systems, we explore how the total energy of converge with respect to the plane-wave basis set as described by the cut-off energy cut-off and with respect to the size of the  $k$ -points mesh for the Brillouin zone integration.

We calculate the total energy of various bulk systems as a function of cut-off energy, which ranging from 300 to 600 eV with a step size of 50 eV and as a function of  $k$ -points scaling from a  $10 \times 10 \times 10$  to a  $55 \times 55 \times 55$  mesh with a step size of 5. We find that a convergence of the total energy to below 5 meV/atom, requires a cut-off energy of 500 eV and a  $35 \times 35 \times 35$   $k$ -point mesh. Fig 2.1 as an example, show the parameter convergence for bulk FeS.

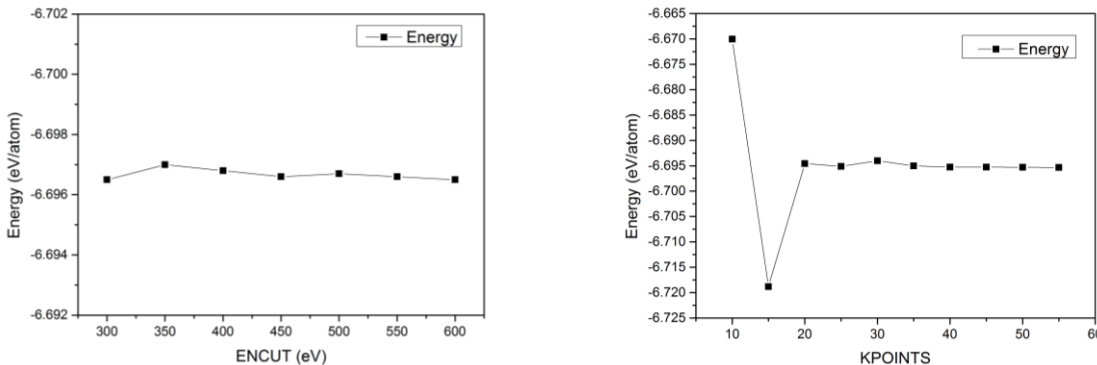


Fig 2.1 Convergence of the total energy with respect to cutoff energy (left) and  $k$ -point mesh size (right) for bulk iron sulfide

$k$ -point sampling with  $35 \times 35 \times 35$ , which the convergence is below 5meV between two steps. Fig. 2.1, as an example, shows how the parameter convergence for bulk FeS works.

### 2.2.2. Energetic stability-formation energy $E_f$

Following the convergence study, we apply the DFT method to determine the energetic stability of the 2D materials. The energetic stability of the 2D materials is given by the difference of its energy relative to the lowest possible energy of a material with the same composition. Note that this lowest energy material may consist of multiple phases. Once the optimized structures and the stability of the

two-dimensional materials are determined, we will characterize the properties of 2D materials.

The DFT calculations start from the candidate structures. Fig 2.2 shows the five candidates two-dimensional structures that exhibit the composition ratio of 1:1 for the single-layer mono-chalcogenides and pnictides. All five candidate structures are either reported for previously synthesized 2D materials or predicted ones <sup>[18]</sup>. Some of these structures exist as individual layers in the layered bulk counterpart structures mentioned above. Therefore we choose the five candidate structures as follow: planar hexagonal, buckled hexagonal, inverted-litharge, litharge and distorted-NaCl. Fig 2.2 illustrates the top and side view of five two-dimensional candidate structures for the MX compounds, with the red sphere indicating the metal element, e.g. Fe and the yellow sphere indicating the non-metal element, e.g. chalcogen atoms.

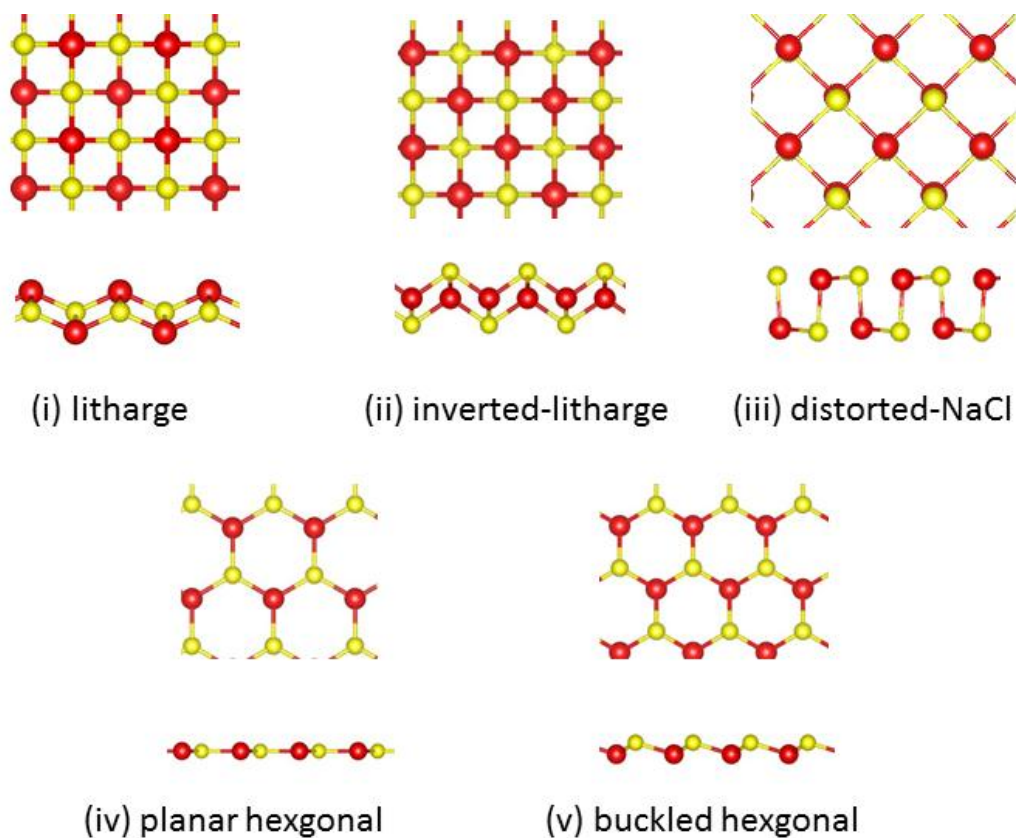


Fig 2.2 Top and side view of the (i) litharge, (ii) inverted litharge, (iii) distorted-NaCl, (iv) planar hexagonal, and (v) buckled hexagonal structures.

Nonoselov and Geim discovered in 2004 that two-dimensional materials such as graphene could be exfoliated from their “parents” bulk layered compounds<sup>[2]</sup>. However if no layered structure “parents” structure existed, how could we determine whether a 2D materials structure exists a free-standing single or few-atom thick layer? A recent study by Singh *et al.*, reported that the MX compounds (M=Ge, Sn, Pb X= S, Se, Te) could be stable in a tetragonal litharge structure and investigated their electronic properties for electronic devices. When it comes to their bulk structures, for example, bulk SnO and PbO adopt a litharge structure that consists of buckled layers<sup>[18]</sup>. There are also some other 2D materials isolated from the bulk counterparts: graphite, which consists of stacked graphene monolayers. Scientists also found more candidates, such as GaTe, Bi<sub>2</sub>Se<sub>3</sub><sup>[37]</sup>, which could be “parent” bulk materials. We begin our screening by substituting the cation elements in this structure. This is worthwhile since the group-IV chalcogenides present a similar materials system as the one investigated here.

For the stability of the predicted two-dimensional materials, we include the energetic and the dynamic stability. First, we determine the energetic stability, which is defined as the difference in energy,  $\Delta E$  between the 2D compound and its bulk counterparts.

$$\Delta E = E_{2D}/N_{2D} - E_{\text{bulk}}/N_{\text{bulk}}$$

where  $E_{2D}$  is the energy of the two-dimensional material and  $E_{\text{bulk}}$  is the lowest energy of any mixture of bulk materials with the same composition as the counterpart two-dimensional materials.  $N_{2D}$  and  $N_{\text{bulk}}$  are the numbers of atoms in the respective unit cell.

Previous research has shown that van der Waals interactions are important in order to accurately predict the formation energy of 2D materials, particularly when the bulk materials exhibit layered

structures<sup>[37]</sup>. Therefore, in our calculation of the formation energy, we use a non-local van der Waals exchange-correlation.

In addition to including the effect of van-der-Waals interactions, we also account for the possibility of different magnetically ordered states in the 2D materials. We consider three magnetic states: ferromagnetic (FM), antiferromagnetic (AFM) and nonmagnetic (NM), which refer to states with the same magnetic moments, alternating magnetic moments, and zero magnetic moment on all metal atoms, respectively. For the distorted rocksalt and litharge-type 2D structures, the unit cell contains 2 iron atoms. We can determine the energy of all three magnetic states by varying the initial magnetic moments in the DFT calculations through the input parameter  $MAGMOM = 2\ 2, 2\ -2,$  and  $0\ 0$  for the FM, AFM, and NM configurations

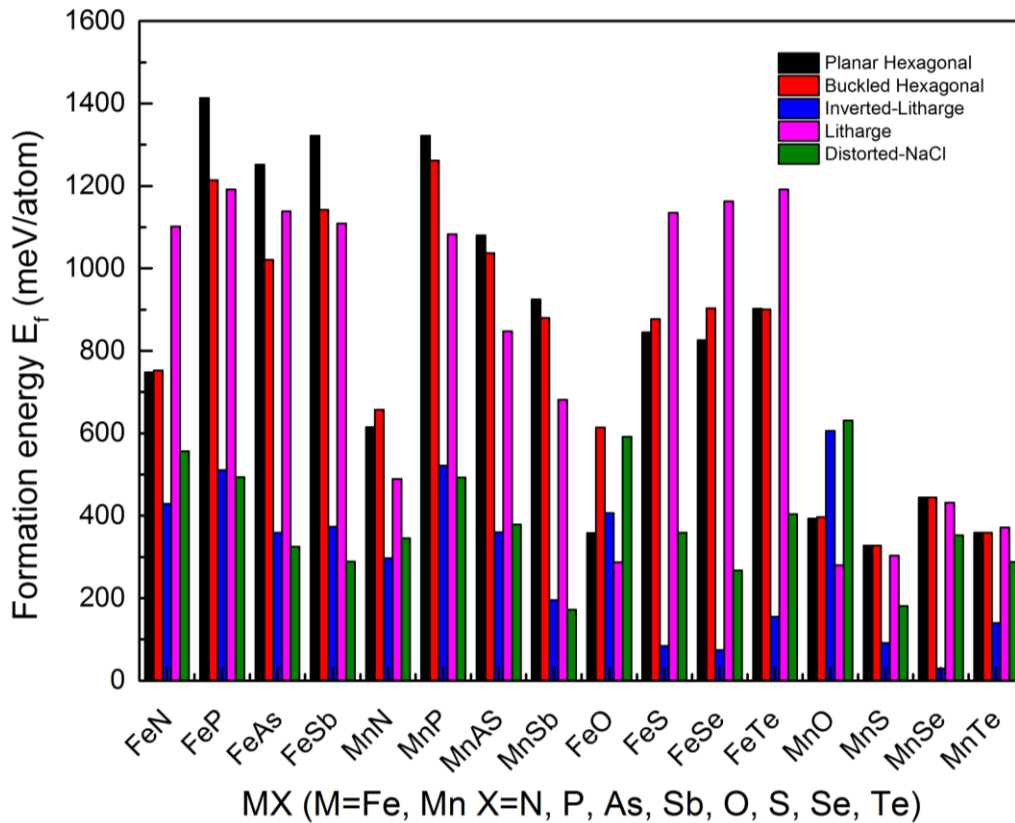


Fig 2.3 Formation energy of all the compounds within the five 2D structure types. The formation energy is defined relative to the energy of the competing bulk structures.

Fig 2.3 shows the formation energies of all Mn and Fe mono-chalcogenide and pnictide compounds for each of the five candidate structure types, indicated by the different colors. The 80 DFT formation energy calculations show that the hexagonal structures, both planar and buckled hexagonal ones among the structures with the highest formation energies ( $> 400$  meV/atom) for the 2D Mn and Fe mono-chalcogenides and pnictides. The inverted litharge and distorted rocksalt structures are among the lowest energy structures.

To determine which of the 2D MX compounds have formation energies low enough to be accessible in synthesis experiments, we compare the formation energies with those of other 2D materials that have previously been synthesized. Fig 2.4 illustrates several synthesized or predicted 2D materials<sup>[40]</sup>. The blue bars indicate experimentally synthesized 2D materials, while the red ones indicate predicted materials. We observe that 2D materials that have been synthesized as free-standing materials all share a similarity, which is that the formation energy is lower than about 200 meV/atom. Thus, we select an empirical cutoff value for our screening of 2D materials of  $E_f < 200$  meV/atom to identify whether there is a good chance to get a free-standing 2D material. Based on the formation energy criteria, we divide the sixteen compounds into three groups according to their formation energies: high, intermediate and low as shown in Table 2.3.

Figure 2.5 shows the 2D compounds with formation energies below 200 meV/atom and compares their formation energies with the values of MoS<sub>2</sub> and graphene. We find that 2D MnSb is most stable in the distorted-rocksalt structure and the six mono-chalcogenides FeS, FeSe, FeTe, MnS, MnSe, and MnTe are stable in the inverted litharge structure.

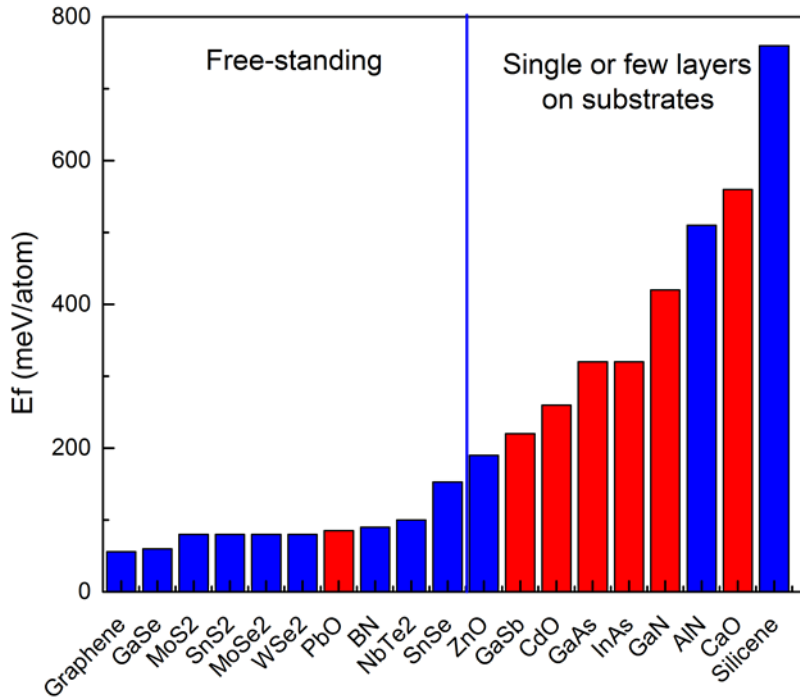


Fig 2.4 Formation energies of synthesized and theoretically predicted 2D materials, blue bar indicates the synthesized one, red bar indicates the predicted ones. (Formation energies of graphene computed using quantum Monte Carlo simulations<sup>[39]</sup>; BN<sup>[40]</sup> and silicone<sup>[40]</sup> were using the LDA exchange-correlation functional; GaSe,<sup>[5]</sup> CrS<sub>2</sub>,<sup>[7]</sup> MoS<sub>2</sub>,<sup>[41]</sup> MoSe<sub>2</sub>,<sup>[41]</sup> WSe<sub>2</sub>,<sup>[41]</sup> NbTe<sub>2</sub>,<sup>[41]</sup> SnS<sub>2</sub>,<sup>[10]</sup> SnS,<sup>[18]</sup> and PbO<sup>[18]</sup> using a van der Waals functional; CdO,<sup>[42]</sup> CaO,<sup>[42]</sup> ZnO,<sup>[42]</sup> GaSb,<sup>[43]</sup> InAs,<sup>[43]</sup> GaN,<sup>[43]</sup> and AlN<sup>[43]</sup> using a GGA functional)

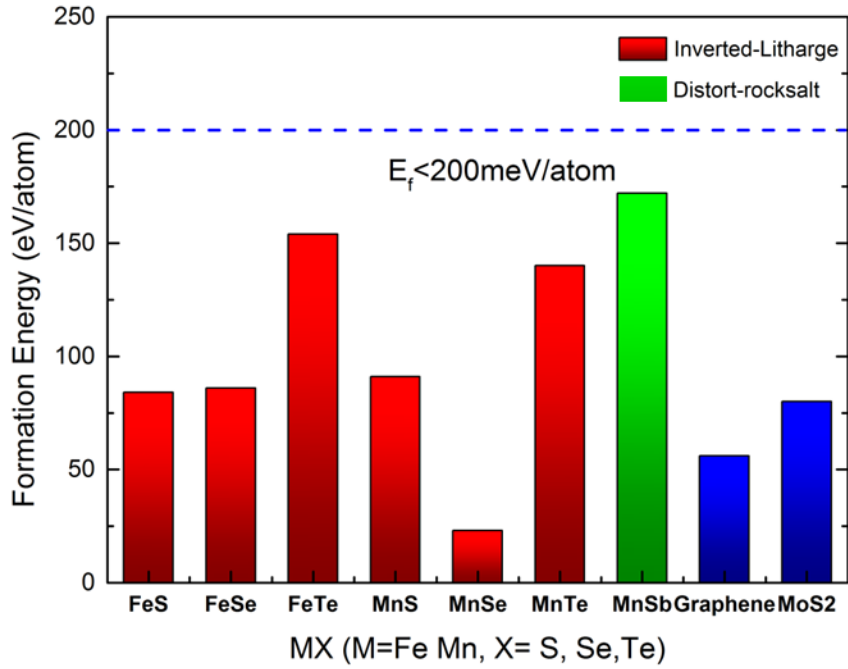


Fig 2.5 Formation energies of MX (M = Fe, Mn X = S, Se, Te) MnSb and well-known 2D materials, graphene and MoS<sub>2</sub>

Table 2.3 classification of formation energy  $E_f$

	Formation energy	Predicted synthesis	selected
High $E_f$	> 400 meV/atom	Unlikely	Not
Intermediate $E_f$	~ 200-400 meV/atom	On substrates	Not focus
Low $E_f$	< 200 meV/atom	Free-standing	Yes

Several additional candidate 2D materials display formation energies between 200 and 400 meV/atom. These 2D materials could possibly be synthesized on substrates and should be considered for further studies of their properties in future work. Here we focus on the seven candidate 2D materials with low formation energies (< 200 meV/atom). Thus, we select the six Mn and Fe mono-

chalcogenide compounds that are stable in the 2D inverted-litharge structure and MnSb, which is stable in the distorted-rocksalt structure and exhibits a magnetic moment of  $2.7\mu_B$  per Mn atom.

Among all the candidates, single-layer MnSe has the lowest formation energy of only 23 meV/atom. This is even lower than the formation energy of graphene and 2H-MoS<sub>2</sub>. In other words, the 2D inverted-litharge MnSe should be easily synthesized by some experimental methods. The 2D structures of FeS, FeSe, and MnS have formation energies similar to that of 2H-MoS<sub>2</sub> and should also be accessible by various synthesis techniques. FeTe, MnTe, and MnSb have higher formation energies comparable to that of 2D SnSe and might be more difficult to grow in single-layer form.

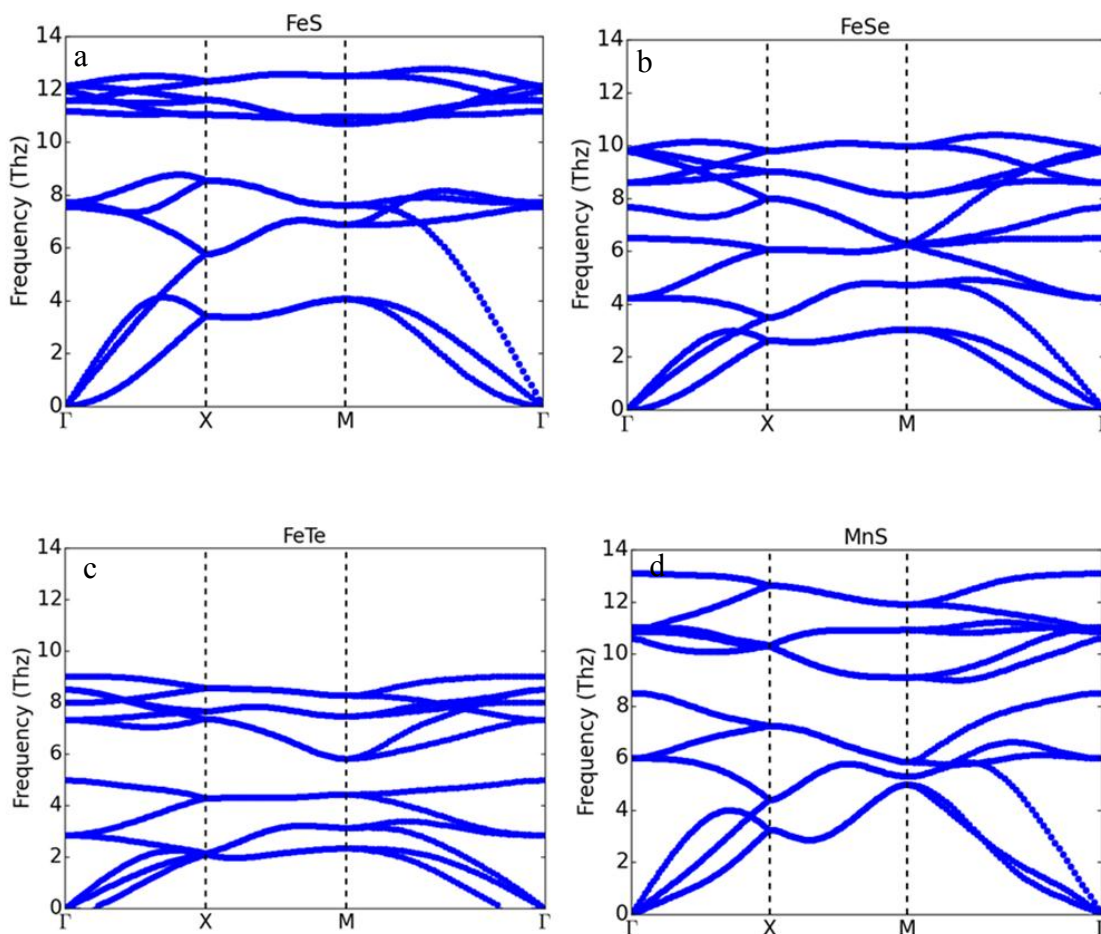
Before exploring the electronic and magnetic properties of these seven 2D materials in Chapters 2.4, 3 and 4, we need to confirm that these compounds are dynamically stable.

### ***2.3. Dynamical stability-phonon spectrum***

The minimization of the energy of a given crystal structure by relaxation is necessary but not sufficient to guarantee the stability of a compound. In order to determine if a compound is dynamically stable, i.e. does not correspond to a saddle point or maximum in configuration space, we need to determine the response of the energy to small structural distortion. The ideal approach to determine the dynamical stability is the calculation of the phonon spectrum for the relaxed single-layer MX compounds.

We are using Phonopy<sup>[44]</sup> with force constants calculated by density-functional-perturbation-theory (DFPT) in VASP. The force constants are calculated using a supercell of the structure. Phonopy applies a Fourier interpolation to calculate the full phonon dispersion. A compound is dynamically stable if all of its phonon modes are real. In other words, no imaginary branches should be presented in the phonon spectrum.

Figure 2.6 shows, the calculated phonon spectra of the 2D MX compounds with their lowest formation energy structures. All the two-dimensional MX compounds presented in the Fig 2.6 have no imaginary branches, which mean they are dynamical stable. However there are some small regions near  $\Gamma$ -point that display slightly imaginary frequencies. These slightly imaginary modes are unlikely to indicate a dynamical instability. Previous studies have seen similar effects and attributed them to several factors <sup>[43, 45]</sup>: (i) the numerical precision could be insufficient or the k-point mesh is not dense enough to calculate the forces responsible for the phonon modes in these regions with sufficient accuracy, (ii) the supercell is too small to obtain resolve enough phonons for the Fourier interpolation.



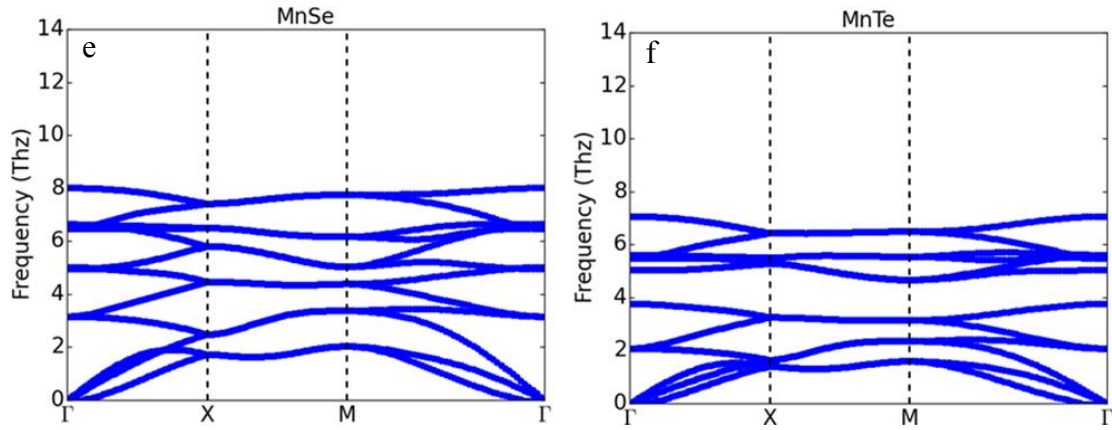


Fig 2.6 Phonon spectra for inverted-litharge MX (M = Fe, Mn X = S, Se, Te) compounds. (a) FeS (b) FeSe (c) FeTe (d) MnS (e) MnSe (f) MnTe

## 2.4 Electronic property

The capability of accurately and efficiently computing and predicting various properties of materials, such as electronic, optical, and mechanical properties is one of the important theoretical breakthroughs of the 20<sup>th</sup> century<sup>[46]</sup>. DFT provides one of the most widely used methods for computational materials characterization.

Following the investigation of the 2D structure stability, we study the electronic properties of the 2D MX compounds (M = Mn, Fe X=S, Se, Te) family. Taking possible spin-polarization into consideration, we find that FeS, FeSe, FeTe and MnS are non-magnetic compounds. To calculate the band structure, we apply the GGA-PBE and the hybrid functional (HSE06). The computationally more expensive hybrid functional includes a fraction of exact exchange, which corrects for the localization and self-interaction error of local and semi-local approximations to the exchange-correlation functional such as and improves the accuracy of the electronic band gap prediction. In other words, DFT calculations with local and semi-local functionals usually underestimate the electronic band-gap, while hybrid functionals overcome this issue through the incorporation of exact exchange. A previous report

from H.L. Zhuang and R.G. Hennig <sup>[10]</sup> compare the band gap values calculated from different functionals with the experimental values. We found that HSE06 shows a more accurate consistency with the experiments, when compared to the PBE functional.

Table. 2.4 Fundamental indirect and direct band gaps (eV) of single-layer SnS<sub>2</sub> obtained from three different approaches. Experimental optical band gaps are for comparison (data from Ref. 10)

Band gap	PBE	HSE06	$G_0W_0$	Experiment
Indirect	1.57	2.52	2.88	2.23
Direct	1.81	2.81	3.16	2.55

A typical band structure calculation in DFT consist of two steps: First we calculate an accurate ground state charge density by using a high quality  $k$ -point sampling. Second, we determine the eigenvalues at the desired  $k$ -points of the band structure, using the density obtained in the previous step. The density is kept fixed during this step of the band structure calculation. In the HSE06 calculation, we add some plotting  $k$ -points (zero weight) into the KPOINTS file to get the graph easier. We employ a  $17 \times 17 \times 1$   $k$ -point mesh to calculate the self-consistent charge density. The vacuum spacing between is set to  $18 \text{ \AA}$  to make the effect of interaction between the layers negligible small.

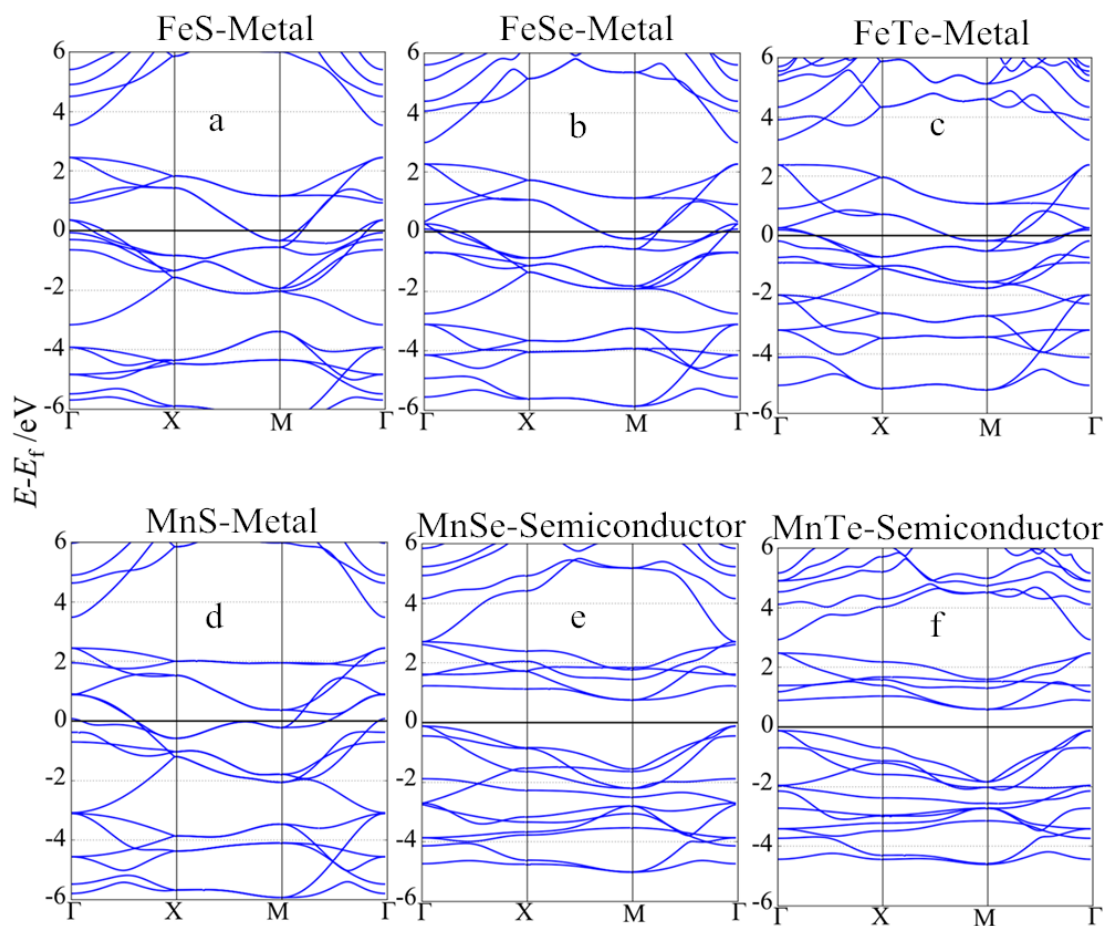


Fig 2.7 PBE band structure calculation for MX (M = Fe,Mn X = S, Se, Te): (a) for FeS (b) for FeSe (c) for FeTe (d) for MnS (e) for MnSe (f) for MnTe

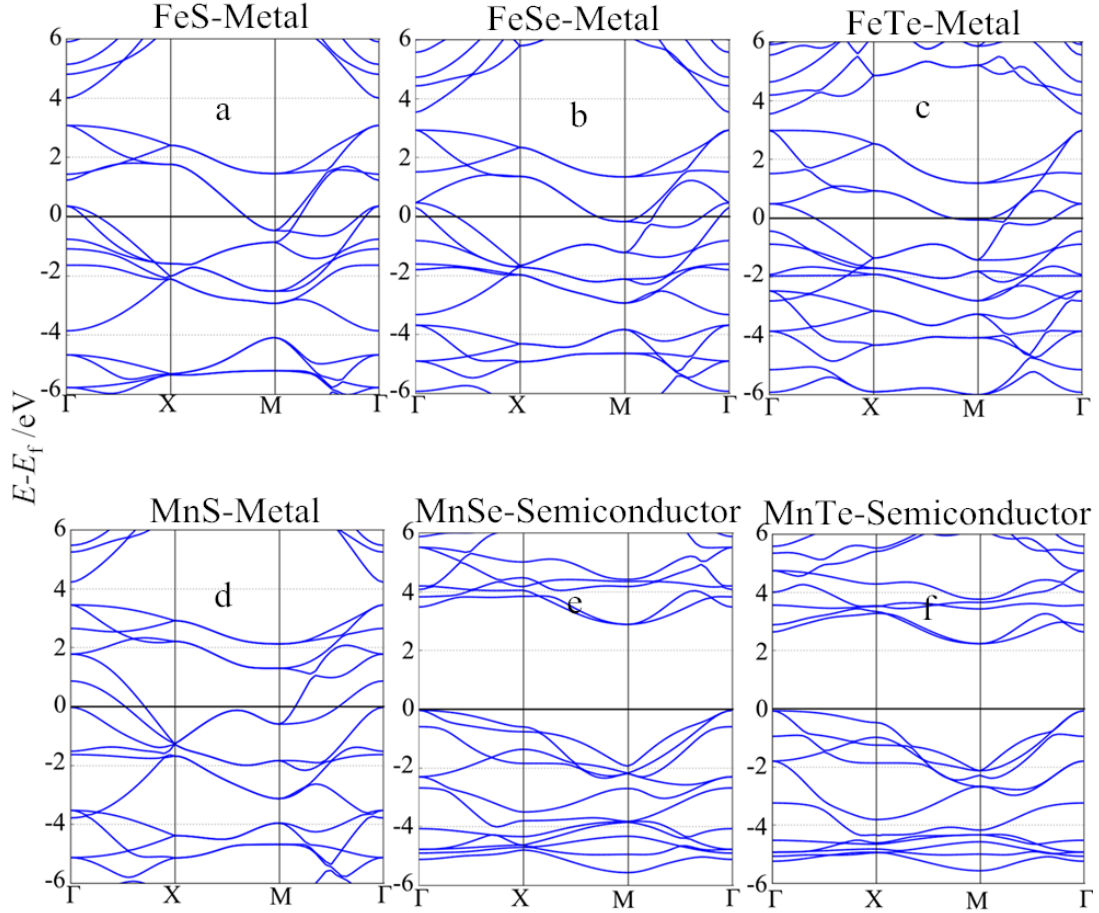


Fig 2.8 HSE06 band structure calculation for MX (M = Fe, Mn X = S, Se, Te): (a) for FeS (b) for FeSe (c) for FeTe (d) for MnS (e) for MnSe (f) for MnTe

The band structure of 2D inverted-litharge MX compounds calculated from both GGA-PBE functionals and HSE06 functionals are shown in Figures 2.7 and 2.8. The Fermi level is set to zero. We find that four of the six single-layer MX chalcogenide compounds are metallic and the other two - MnSe and MnTe - are semiconducting with an indirect band gap from between the  $\Gamma$  and the M-point. The band gaps of MnSe and MnTe are 2.7 eV and 2.1 eV, respectively. The HSE06 functional increases the band gap, compared to the prediction by the PBE functional. Due to the presence of semiconducting band gaps and low formation energy shown by MnSe and MnTe, we further explore the possibility of the photocatalytic activity of the 2D MnSe and MnTe compounds.

## CHAPTER 3

### SINGLE-LAYER Mn MONO-CHALCOGENIDE PHOTOCATALYSTS

#### 3.1 Photocatalytic water splitting

In 1972, Fujima and Honda discovered photocatalytic splitting of water on  $\text{TiO}_2$  electrode [47]. Production of hydrogen from photocatalytic water splitting provides an alternative clean and renewable energy source [48-50]. Therefore, it has been studied extensively over the last four decades. Many studies have focused on understanding the fundamental process, method to improve the photocatalytic efficiency, and the search for alternative photocatalysts.

In a photocatalytic process, incident light of sufficient energy excites an electron across the optical band gap of the semiconducting photocatalysts and generates an electron-hole pair, called excitation. This exciton then needs to diffuse to the solid/water interface and dissociate into an unbound electron and hole. The excited electron then drives the hydrogen reduction reaction generating hydrogen, and the hole participates in the oxidation reaction to generate oxygen. Fig 3.1 illustrates the process of photocatalysis.

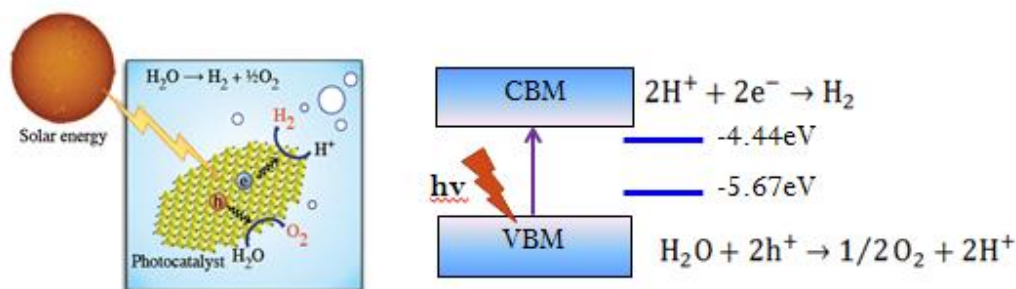
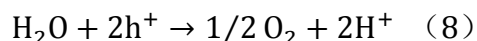
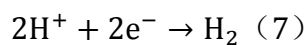


Fig 3.1 Illustration of photocatalytic process. Left figure taken from Ref. 5

The key factor in the photocatalysis is the solar-to-energy conversion efficiency. For example, going from bulk rutile  $\text{TiO}_2$  to  $\text{TiO}_2$  nanotubes boost the solar-to-hydrogen conversion efficiency from 2.2%<sup>[50]</sup> to 16%<sup>[51]</sup>, remarkable improvement. 2D materials exhibit two potential advantages that could lead to an enhanced efficiency as photocatalyst<sup>[52]</sup>. First, 2D materials maximize the surface area per amount of material, thus exhibit a high specific surface area available for photocatalytic reactions. Second, the ultimate scale of 2D materials minimizes the distance that photo-generated electrons and holes have to migrate before reaching the solid/water interface, reducing the possibility of electron and hole recombination. Thus improve the performance<sup>[52]</sup>.

DFT can determine several intrinsic materials properties to screen semiconductors for their potential as water-splitting photocatalysts. There are several intrinsic criteria for a 2D semiconductor to become a candidate for water splitting<sup>[5]</sup>. Low formation energy, ensures the possibility to synthesize the materials. The band gap must be larger than 1.23 eV for the electron and hole to have sufficient energy to drive the water splitting works but the band gap should be smaller than 3 eV to absorb enough sun light. The band-edges, valence band maximum (VBM) and conduction band minimum (CBM) must straddle the water redox potential as illustrated in Figure 3.1. The material should be insoluble in water. Other criteria include small exciton binding energy, low rate of backward reaction etc<sup>[5]</sup>. A.K. Singh, R.G.Hennig's previous work<sup>[52]</sup> provides a detailed description of the criteria and a discussion of how DFT methods can estimate a 2D material's potential as a photocatalyst.

### ***3.2 Single-layer MnSe and MnTe***

As mentioned in the previous chapter, two-dimensional inverted-litharge MnSe and MnTe show quite low formation energies of less than 200 meV/atom - an empirical value for likely free-standing

single-layer materials. This indicates that MnSe and MnTe are potentially easy to synthesize in a single-layer and free-standing form. Moreover both of these two systems are dynamical stable. The phonon spectra of these two systems are in Figure 2.6.

We also apply the HSE06 hybrid functional to accurately estimate the 2D candidate materials' band gaps. We predict that MnSe and MnTe have an indirect band-gap from  $\Gamma$  to M of 2.6 eV and 2.1 eV. This is within the range of 1.23 eV to 3 eV, required for photocatalysis. However, the band gap is not a direct band gap, which might slightly reduce the adsorption efficiency. For the MnTe, we also find a direct band gap at the  $\Gamma$ -point, which is 2.4 eV – close to the indirect band gap. It will also help improve the absorption efficiency.

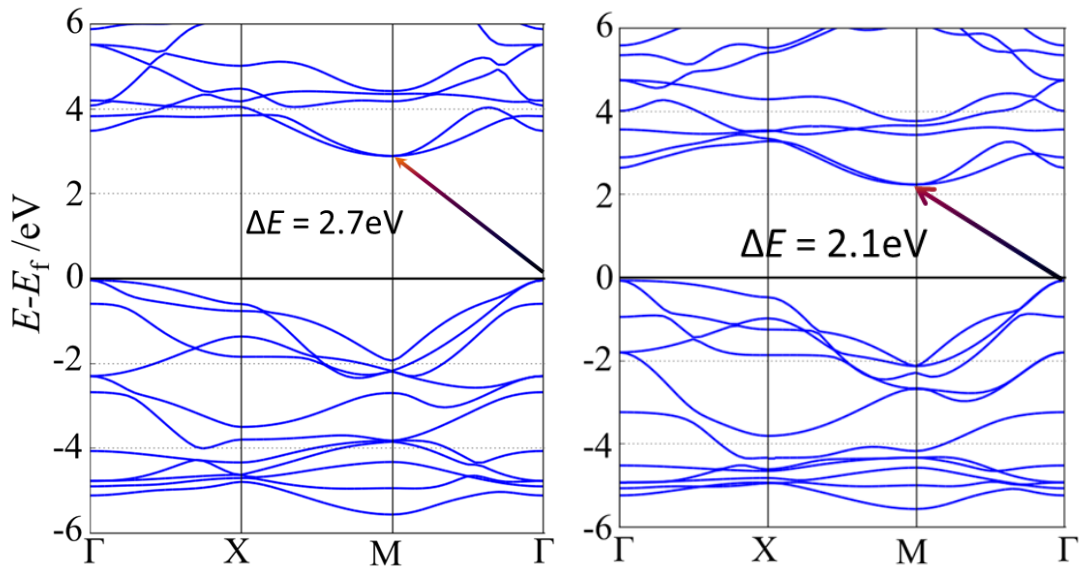


Fig 3.2 HSE06 band structure for MnSe and MnTe showing that both materials exhibit an indirect band gap.

To determine the band edge positions of the 2D materials and compare them with the water redox potentials, we need to align the electrostatic potential in the vacuum region. Figure 3.3 and 3.4 show the electrostatic potential as a function position perpendicular to the layers and averaged within the planes parallel to the 2D materials. We calculate the electrostatic potential in the vacuum region by

taking the value in the middle of the vacuum region. The vacuum potential of MnSe or MnTe is 2.6 and 3.3 eV respectively. We next compare the vacuum level with the energy of the valence band maximum and conduction band minimum to obtain the work functions and electron affinities of these two single-layer materials.

The valence band maximum and conduction band minimum of unstrained single-layer MnSe and MnTe relative to the vacuum level are compared to the water redox potential in Figure 3.6 and Table 3.1. We find that the VBM and CBM of MnSe straddle the redox potentials of water at pH=0 and pH=7. For MnTe, the VBM is slightly above the oxygen evolution potential. However, at higher pH, the shift in the redox potentials results in a favorable alignment of the VBM and CBM with the water redox potentials and makes MnTe a potential photocatalyst.

Table 3.1 energy summarization of water splitting

	ph=0	ph=7
H <sup>+</sup> /H <sub>2</sub>	-4.44 eV	-4.02 eV
O <sub>2</sub> /H <sub>2</sub> O	-5.67 eV	-5.26 eV
	VBM	CBM
MnSe energy level	-6.33 eV	-3.57 eV
MnTe energy level	-5.64 eV	-3.53 eV

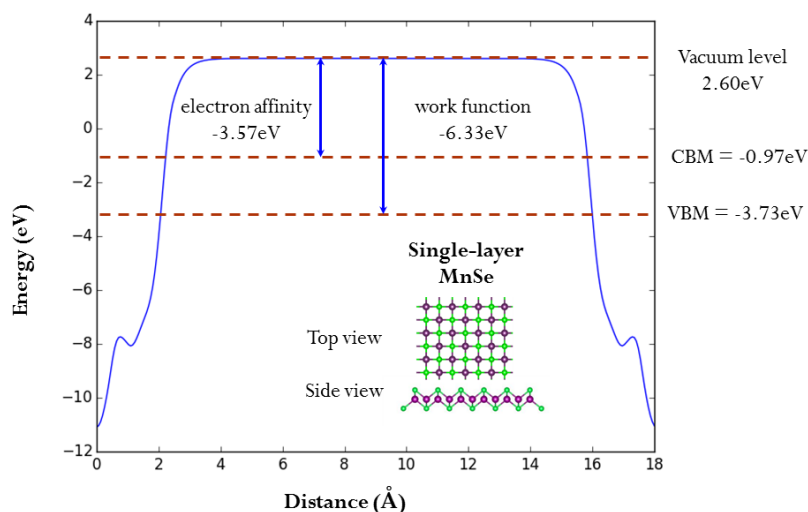


Fig 3.3 Electrostatic potential at vacuum level to determine the workfunction and electron affinity of

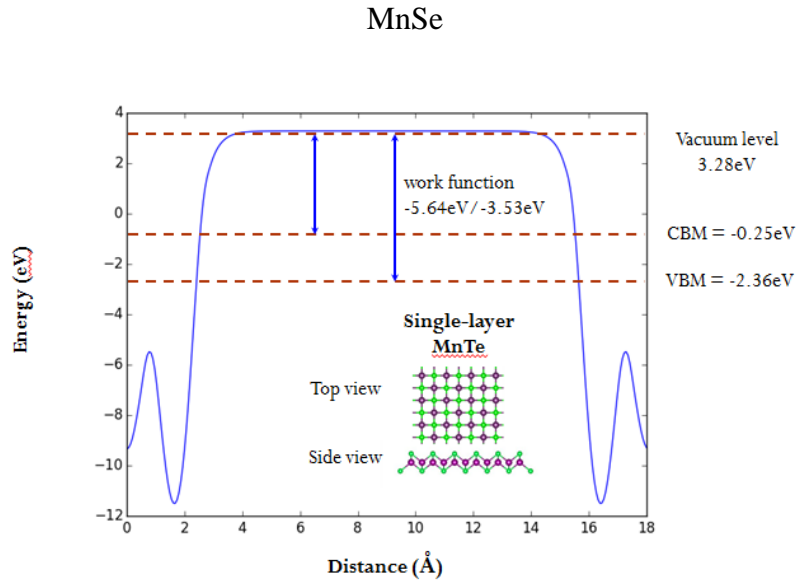


Fig 3.4 Electrostatic potential at vacuum level to determine the workfunction and electron affinity of

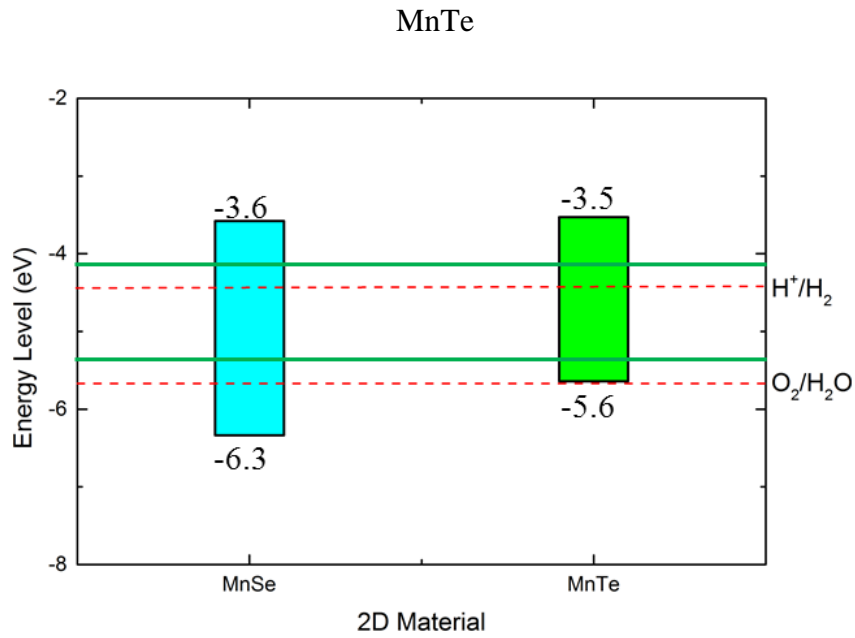


Fig. 3.5 Band edge positions of single-layer MnSe and MnTe relative to the vacuum level at zero strain show that both 2D materials are potential photocatalysts.

In summary, we find that the single-layer MnSe and MnTe have low formation energies of 23 and 140 meV/atom, respectively, and are dynamically stable, which make these materials potentially

easy to synthesize. Their electronic structure shows that both 2D materials have a favorable band alignment with the redox potential of water, making them candidates for the photocatalytic water splitting.

## CHAPTER 4

### MAGNETIC BEHAVIOUR OF TWO-DIMENSIONAL MnSb

#### **4.1 Introduction**

The magnetic properties of materials are controlled by their electronic structure and provide the foundation for the materials' application in devices ranging from energy conversion, to data storage, and electronics. The magnetic properties of materials are divided into five main groups: diamagnetic, paramagnetic, ferromagnetic, and antiferromagnetic and ferrimagnetic and are characterized by the magnetic susceptibility  $\chi_m$ , which is defined as the ratio of a materials' magnetization  $\mathbf{M}$  when placed in a magnetic field  $\mathbf{H}$ .

$$\chi_m = \mathbf{H}/\mathbf{M} \quad (9)$$

For diamagnetic materials,  $\chi_m$  is negative and small magnetic susceptibility ( $\sim -10^{-6}$ ), which means the magnetization  $M$  is in the opposite direction to the applied field  $H$ . In other words, the materials try to expel the applied magnetic field. Paramagnetic materials have a positive but small magnetic susceptibility ( $\sim 10^{-5}$ ). The alignment of spins of conduction electrons with the field result in paramagnetism, which is called *Pauli spin paramagnetism*. Ferromagnetic materials have a positive and large magnetic susceptibility due to a quantum mechanical exchange interaction between atoms aligning the electron spins. In contrast, antiferromagnetic materials have a positive and small magnetic susceptibility. Ferrimagnetic materials possess a large and positive magnetic susceptibility. Most of the applications focus on the ferromagnetic and ferrimagnetic properties <sup>[53]</sup>.

DFT methods can calculate the magnetic response of a material. In this work, we determine if the 2D materials display a magnetically ordered structure, i.e. we calculate the energy of non-magnetic, ferromagnetic, and antiferromagnetic configurations. Table 5 summarizes the finding that out of the

seven Mn and Fe compounds, two are antiferromagnetic (MnSe and MnTe) and one is ferromagnetic (MnSb).

Table 4.1 Magnetic properties of 2D MX compounds

2D materials	Magnetic order	Metal or band gap	2D structure
FeS	Non-magnetic	Metal	
FeSe	Non-magnetic	Metal	
FeTe	Non-magnetic	Metal	
MnS	Non-magnetic	Metal	
MnSe	Antiferromagnetic	2.7 eV	
MnTe	Antiferromagnetic	2.1 eV	
MnSb	Ferromagnetic	Metal	

#### 4.2 Two-dimensional ferromagnet MnSb

Bulk MnSb appears in a hexagonal space group  $P6_3/mmc$ . The single-layer MnSb occurs in a distorted rocksalt structure with a square lattice, which shown in Figure 15. The formation energy of 2D MnSb is 172 meV/atom and it is also dynamically stable.

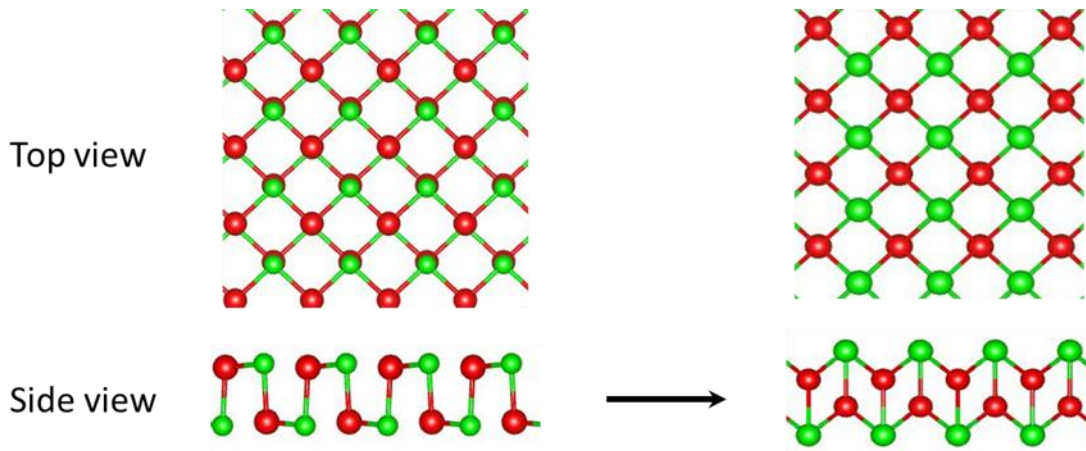


Fig 4.1 Structure relaxation of 2D MnSb in the distorted rocksalt structure.

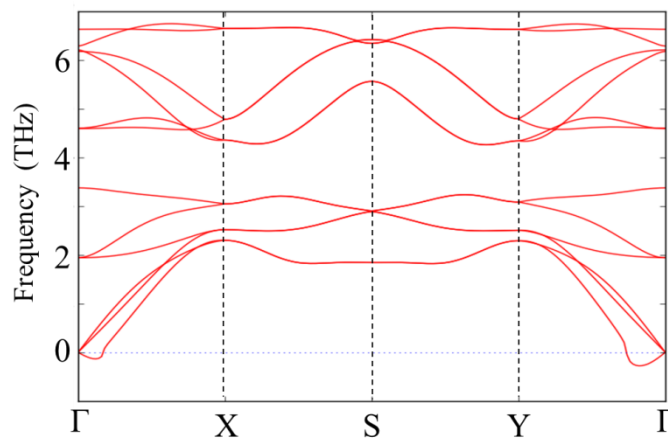


Fig 4.2 Phonon spectrum for two-dimensional MnSb shows that MnSb is stable. The small imaginary modes near the  $\Gamma$  point are likely caused by numerical inaccuracies.

By checking the magnetic moment of MnSb, we apply the ISPIN tag in the input file, and we get a magnetic value of  $5.4 \mu_B$ . It is a ferromagnetic material, having relatively large magnetizations in a non-magnetic field. All the atomic magnetic moments are aligned parallel to each other, or we can say, in the same direction.

Spin-polarized DFT calculations determine that the magnetic moment of MnSb is  $2.7 \mu_B$  per Mn atom. MnSb is a ferromagnetic metal with large magnetizations in a non-magnetic field. All the atomic magnetic moments are aligned parallel to each other, pointing in the same direction.

The isolated Mn atom has an electron structure  $[Ar] 3d^5 4s^2$ , with a partially filled 3d subshell unfilled. Due to Hund's rule, five electrons with the same spin occupy the five 3d orbitals. In the 2D material, the number of electrons on the Mn site is slightly increased due to the difference in electronegativity of the Mn and Sb atom. Also, the electric field of the neighboring atoms in the MnSb structure breaks the spherical symmetry of the Mn sites and d-electron orbitals. As a result, the magnetic moment is lowered from the maximum value of 5 to 2.7 in the 2D MnSb compound.

The ferromagnetic ordering of a material persists up to a maximum temperature, above which it turns into a paramagnetic structure. The critical temperature for this transition is called the Curie temperature  $T_c$ . We estimate the Curie temperature of single-layer MnSb using a Heisenberg model. More details about the Heisenberg model can be found in many text books such as *Solid State Physics* By C. Kittel<sup>[54]</sup>. In the Heisenberg model the energy of a system of spins is given by

$$H = -J \sum_i \sum_j \mathbf{S}_i \mathbf{S}_j \quad (10)$$

where  $\mathbf{S}_i$  and  $\mathbf{S}_j$  are vectors of fixed length that describe the spins of the system and  $J$  is the exchange coupling between the spins. Here we only consider interactions between neighboring spin and hence only include a single coupling term  $J$ . If  $J > 0$  the material shows a ferromagnetic order, while for  $J < 0$  it shows an antiferromagnetic order.

In the Heisenberg model, the Curie temperature is determined by the crystal lattice and the exchange coupling  $J$ , which can be obtained from DFT calculations of the total energy difference of the ferromagnetic and the antiferromagnetic state. In the 2D MnSb compound, the spin on each Mn site is coupled to four neighboring spins on the 4 closest Mn sites. If all spins are aligned, the ferromagnetic energy of the Heisenberg model is

$$E_{FM} = -JS^2 N_z / 2 \quad (11)$$

and if the spins alternate, the antiferromagnetic energy of the model is

$$E_{AFM} = JS^2Nz/2, \quad (12)$$

where  $N$  the number of Mn sites,  $z$  the number of nearest neighbors (four in our case) and  $S$  is the magnitude of the spins. The energy difference between the ferromagnetic and antiferromagnetic state allows us to estimate the exchange coupling  $J$ . From  $\Delta E = E_{FM} - E_{AFM} = JS^2Nz$ , we get  $\frac{\Delta E}{N} = JS^2z$ . The mean-field theory predicts that  $J = \frac{3k_B T_c}{2zS^2}$  and hence,  $T_c = \frac{\Delta E}{N} \frac{2}{3k_B}$ . Table 4.1 shows the values of the energy difference and the prediction of the Curie temperature for 2D MnSb with the PBE and HSE06 functional. The predicted Curie temperature is 820K for the PBE functional and 278K for the HSE functional.

Table 4.2 estimation of Curie temperature

	PBE functional	HSE06 functional
$\Delta E$ (meV/atom)	106	36
Tc (K)	820	278

Magnetic materials can have a variety of applications, such as in magnetic recording media for the data storage and the reading and writing of the information. For recording head applications, the materials have to be magnetically soft in order to magnetize easily by the input current. Commonly used recording heads are Ni-Fe alloys or some magnetic amorphous metals such as CoZrNb. For those used in magnetic storage media, the materials should have high remnant magnetization and a high coercivity as well. However, the calculations of the magnetic anisotropy and coercitivity are computationally demanding and beyond the scope of our work. The differences in the density of states of the spin-up and down channel indicate that the current in 2D MnSb will be highly spin-polarized, which is useful in some spintronics applications.

## CHAPTER 5

### CONCLUSION AND FUTURE WORK

#### *5.1 Conclusion*

In this thesis, we screen the periodic table and search for novel 2D materials by combining Mn and Fe metal elements with chalcogen and pnictogen elements in a 1:1 stoichiometry. We identify the lowest energy structures for these compounds among a set of 5 candidate structures that have previously been observed or predicted for other 2D materials. We identify 6 low energy Fe and Mn compounds out of the list of 16 compounds and 5 structures using a cut-off value of 200 meV/atom for the formation energy of the 2D materials relative to their bulk counterparts. The 5 low-energy compounds in the family of Fe and Mn mono-chalcogenides are stable in the inverted-litharge tetragonal structures. The one compound in the mono pnictides family – MnSb – favors the distorted rocksalt square structure. Both the PBE and the HSE06 exchange-correlation functional predict that the 2D inverted-litharge MnSe and MnTe are semiconductors, with indirect band gaps of 2.7 and 2.1 eV, respectively, while the 4 other inverted-litharge MX compounds are metals. The band edge position of 2D MnSe and MnTe indicate that both materials are suitable candidate materials for photocatalysis. For the ferromagnetic 2D square lattice MnSb, we estimate the Curie temperature using a Heisenberg model. The critical temperature for PBE and HSE06 is 820 and 278K, respectively, showing a possibility for applications of 2D MnSb as a room temperature magnetic metal.

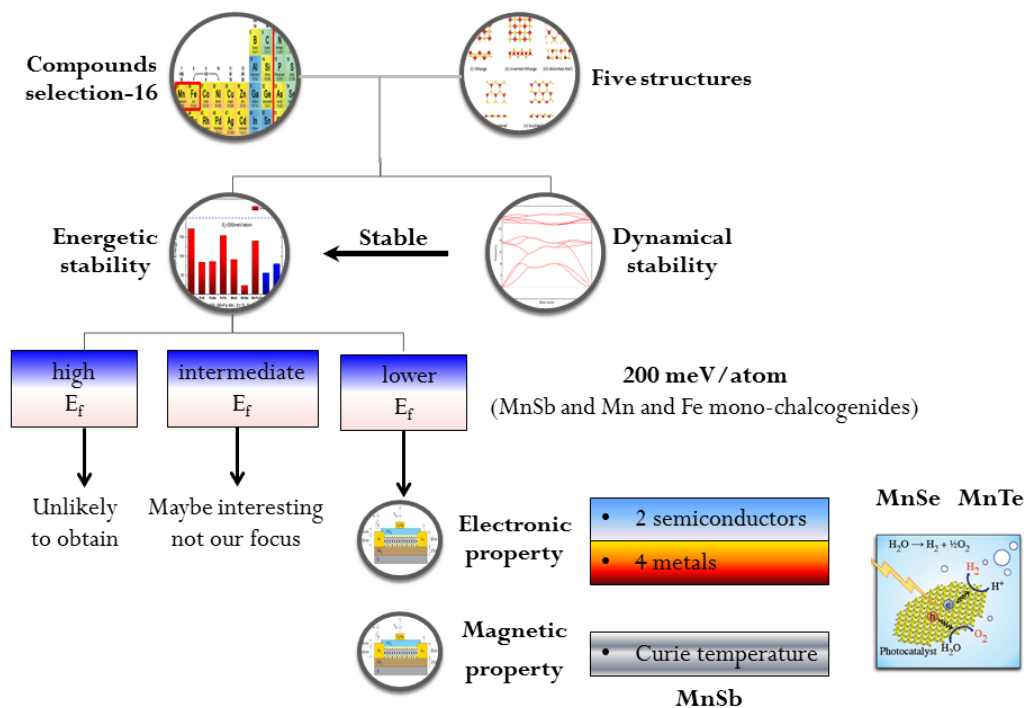


Figure 5.1 The dendrogram of our study

## 5.2 Future work

### 5.2.1 Future searches for novel 2D materials

Since the feasibility of 2D graphene synthesis, two-dimensional materials draw particular interests in materials science field. Some  $MX_2$ , such as 1T- $FeS_2$ , 1T- $NiS_2$ , shows either a half-metallic or semiconducting properties, which is interesting when it comes to the device applications. As a result, it is worthwhile trying other transitional metal sulfide or mono-chalcogenides to check various magnetic properties. Moreover there are also a large number of 2D members that we do not identify, e.g. transitional metal oxides. The searches for novel 2D materials should be extended to other crystal structures and compositions by exploring the configuration space using genetic algorithms.

### 5.2.2 Water solubility for the predicted photocatalysts

Based on the fact of working in the water environment, the solubility and the corrosion of 2D materials in electrolytes need more attention to understand the way of improving the efficiency. A

previous study from R. Hennig's group presented a Pourbaix Diagrams to represent aqueous phase electrochemical equilibria. The diagram indicates the stability boundaries for dominant solution as a function of pH and applied electrical potential [52]. By screening other 2D materials for their stability in

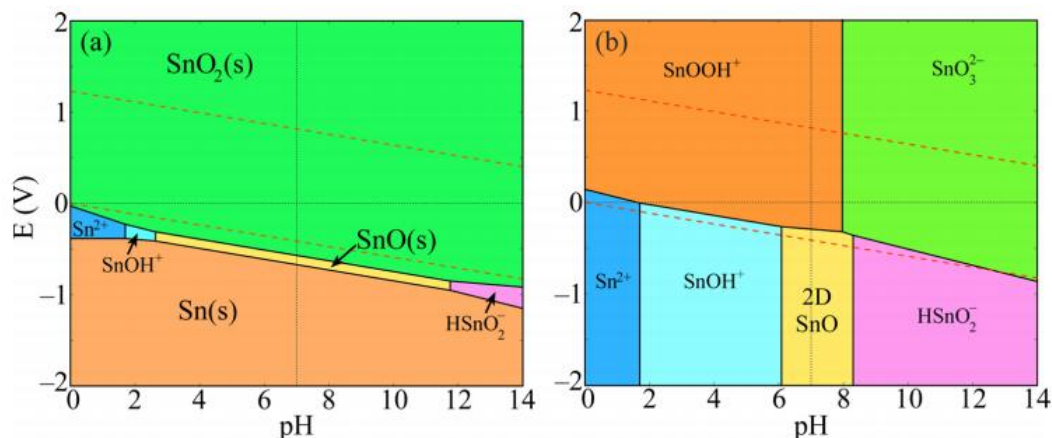


Figure 5.2 illustration of stability of SnO in water

(a) Pourbaix diagram showing the range of stability for the bulk phases Sn, SnO, and SnO<sub>2</sub> (b) Stability of 2D SnO in water against dissolved species

water and corrosion resistance using Pourbaix diagrams, we could determine their suitability for application in aqueous environments such as in fuel cells, as photocatalysts, and protective coatings.

Overall, the future seems bright for 2D materials, with many more materials awaiting discovery whose properties will provide new and exciting opportunities for materials research and applications for years to come.

## REFERENCES

- [1]. “This Month in Physics History: October 22, 2004: Discovery of Graphene”. *APS News*. Series II **18** (9): 2. 2009
- [2]. K.S.Novoselov, A.K. Geim, S.V. Morozov, D. Jiang, Y. Zhang, S.V. Dubonos and A.A. Firsov, *Science* **306**, 666 (2004)
- [3]. N.Alem, R.Erni, C.Kisielowski, M.D. Rossell, W. Gannett and A. Zettl, *Phys. Rev. B* **80**, 155425 (2009)
- [4]. C. Tusche, H.L. Meyerheim and J. Kirschner, *Phys. Rev. Lett.* **99**, 026102 (2007)
- [5]. H.L. Zhuang and R.G. Hennig, *Chem. Mater.* **25**, 3232 (2013)
- [6]. K.F. Mak, C. Lee, J. Hone, J. Shan and T.F. Heinz, *Phys. Rev. Lett.* **105**, 136805 (2010)
- [7]. H.L. Zhuang, R.G. Hennig, M.N. Blonsky and M.D. Johannes, *Applied Physics Letters* **104**, 022116 (2014)
- [8]. Q.H. Wang, K. Kalantar-Zadeh, A. Kis, J.N. Coleman, and M.S. Strano, *Nature Nanotechnology* **7**, 699 (2012)
- [9]. S.L. He, J.F. He, L. Zhao, D.F. Liu, X.L. Dong, X. Liu, D.X. Mou, Y.Y. Peng, Y. Liu, C.Y.Chen, G.D. Liu, and X.J. Zhou, *Nature Materials* **12**, 605 (2013)
- [10]. H.L. Zhuang, R.G. Hennig, *Phys. Rev. B* **88**, 115314 (2013)
- [11]. Y.F. Sun, H. Cheng, S. Gao, Z.H. Sun, Q.H. Liu, T. Yao, S. Q. Wei, and Y. Xie, *Angew. Chem. Int. Ed.* **51**, 8727 (2012)
- [12]. F. Bonaccorso, A. Lombardo, T. Hasan, Z.P. Sun, L. Colombo and A.C. Ferrari, *Materials Today*, **15**, 564 (2012)
- [13]. R.Y. Yue, A.T. Barton, H. Zhu, A. Azcatl, L.F. Pena, J. Wang, R. M. Wallace, C.L. Hinkle *et al.* *ACS Nano* **9**, 474 (2015)
- [14]. H.L. Zhuang, R.G. Hennig, *Journal of Metals* **66**, 366 (2014)
- [15]. S. V. Morozov, D. Jiang, F. Schedin, T.J. Booth, A. K. Geim ,V.V. Khotkevich, and K.S. Novoselov, *PNAS*, **102**, 10451 (2005)
- [16]. Z.H. Zhang, Y. Yang, F.B. Xu, L.Q. Wang, and B.I. Yakobson, *Adv. Funct. Mater.* **25**, 367 (2015)

- [17]. L. Ao, H.Y. Xiao, X.Xiang, S. Li, K.Z. Liu, H. Huang, and X.T. Zu, *Phys. Chem. Chem. Phys.*, **17**, 10737 (2015)
- [18]. A. K. Singh, R.G. Hennig, *Applied Physics Letters* **105**, 042103 (2014)
- [19]. D. Sholl, J.A. Steckel, *Density Functional Theory: A Practical Introduction*
- [20]. J. G. Lee, *Computational Materials Science: An Introduction*, CRC Press, 2012
- [21]. J.P. Perdew and A. Zunger. Self-interaction correction to density-functional approximations for many-electron systems. *Phys. Rev. B*, **23**, 5048 (1981)
- [22]. J.P. Perdew, J.A. Chevary, S.H. Vosko, K.A. Jackson, M.R. Pederson, D.J. Singh, and C. Fiolhais. Atoms, molecules, solids, and surfaces: Applications of the generalized gradient approximation for exchange and correlation. *Phys. Rev. B*, **46**, 6671 (1992)
- [23]. J.P. Perdew, J.A. Chevary, S.H. Vosko, K.A. Jackson, M.R. Pederson, D.J. Singh, and C. Fiolhais. Erratum. Atoms, molecules, solids, and surfaces: Applications of the generalized gradient approximation for exchange and correlation. *Phys. Rev. B*, **48**, 4978 (1993)
- [24]. J. P. Perdew, K. Burke, and M. Ernzerhof. Generalized gradient approximation made simple. *Phys. Rev. Lett.*, **77**, 3865 (1996)
- [25]. J. P. Perdew, K. Burke, and M. Ernzerhof. Erratum: Generalized gradient approximation made simple. *Phys. Rev. Lett.*, **78**, 1396 (1997)
- [26]. G. Kresse and J. Hafner. Ab initio molecular dynamics for liquid metals. *Phys. Rev. B*, **47**, 558 (1993)
- [27]. G. Kresse and J. Hafner. Ab initio molecular-dynamics simulation of the liquid-metal-amorphous-semiconductor transition in germanium. *Phys. Rev. B*, **49**, 14251 (1994)
- [28]. G. Kresse and J. Furthmüller. Efficiency of ab-initio total energy calculations for metals and semiconductors using a plane-wave basis set. *Comput. Mat. Sci.*, **6**, 15 (1996)
- [29]. G. Kresse and J. Furthmüller. Efficient iterative schemes for ab-initio total-energy calculations using a plane-wave basis set. *Phys. Rev. B*, **54**, 11169 (1996)
- [30]. M. Dion, H. Rydberg, E. Schröder, D.C. Langreth, and B.I. Lundqvist, *Phys. Rev. Lett.* **92**, 246401 (2004).

- [31]. G. Román-Pérez, J.M. Soler, *Phys. Rev. Lett.* **103**, 096102 (2009)
- [32]. J. Klimeš, D.R. Bowler, and A. Michaelides, *J. Phys.: Cond. Matt.* **22**, 022201 (2010).
- [33]. T. Thonhauser, V.R. Cooper, L. Shen, A. Puzder, P. Hyldgaard, and D.C. Langreth, *Phys. Rev. B* **76**, 125112 (2007)
- [34]. J. Paier, M. Marsman, K. Hummer, G. Kresse, I.C. Gerber, J. G. Angyan, *J. Chem. Phys.* **124**, 154709 (2006)
- [35]. A. Jain, S.P. Ong, G. Hautier, W. Chen, W.D. Richards, S. Dacek, S. Cholia, D. Gunter, D. Skinner, G. Ceder, K.A. Persson, *Applied Physics Letters Materials*, 2013, **1**(1), 011002.
- [36]. H.L. Zhuang, R.G. Hennig, M.N. Blonsky and M.D. Johannes, *Applied Physics Letters* **104**, 022116 (2014)
- [37]. V. Nicolosi, M. Chhowalla, M.G. Kanatzidis, M. S. Strano, and J.N. Coleman, *Science*, **340**, 1226419 (2013)
- [38]. M.C. Payne, M.P. Teter, D.C. Allan, T.A. Arias, and J.D. Joannopoulos, *Review of Modern Physics*, **64**, 1046 (1992)
- [39]. L. Spanu, S. Sorella, and G. Galli. *Phys. Rev Lett.* **103**, 196401 (2009)
- [40]. H.L. Zhuang, R.G. Hennig, *Appl. Phys. Lett.* **101**, 153109 (2012)
- [41]. H.L. Zhuang, R.G. Hennig, *J. Phys. Chem. C*, **117** 20440 (2013)
- [42]. H.L. Zhuang, R.G. Hennig, *Appl. Phys. Lett.* **103**, 212102 (2013)
- [43]. H.L. Zhuang, A.K. Singh, and R.G. Hennig, *Phys. Rev. B*, **87** 165415 (2013)
- [44]. A. Togo, F. Oba, and I. Tanaka, *Phys. Rev. B*, **78**, 134106 (2008)
- [45]. C. Ataca et al. *J.Phys.Chem. C*, 116 (2012)
- [46]. National Research Council (US) Committee on Challenges for the Chemical Sciences in the 21st Century. *Beyond the Molecular Frontier: Challenges for Chemistry and Chemical Engineering*. Washington (DC): National Academies Press (US); 2003. **6**, *Chemical Theory and Computer Modeling: From Computational Chemistry to Process Systems Engineering*
- [47]. A. Fujishima, K. Honda, *Nature* **238**, 37 (1972)
- [48]. M. Gratzel, *Nature* **414**, 338 (2001)

- [49]. M.G. Walter, E.L. Warren, J.R. McKone, S.W. Boettcher, E.A. Santori, and N.S. Lewis, *Chem. Rev.* **110**, 6446 (2010)
- [50]. X. Chen, S. Shen, L. Guo, and S.S. Mao, *Chem. Rev.* **110**, 6503 (2010)
- [51]. Y.J. Lin, G.B. Yuan, R. Liu, S. Zhou, S. W. Sheehan, D.W. Wang, *Chem. Phys. Lett.* **507**, 209 (2011)
- [52]. A. K. Singh, K. Mathew, H.L. Zhuang, and R.G. Hennig, *J. Phys. Chem. Lett.* **6**, 1087 (2015)
- [53]. S.O. Kasap, *Principles of Electronic Materials and Devices: Third Edition*
- [54]. C. Kittel, *Introduction to Solid State Physics: Eighth Edition*
- [55]. J. Park, B.D. Yu, and S. Hong, *Current Applied Physics.* **15**, 8, 885 (2015)
- [56]. G.I. Csonka, J.P. Perdew, A. Ruzsinszky, P.H.T. Philipsen, S. Lebegue, J. Paier, O.A. Vydrov, J.G. Angyan, *Phys. Rev. B* **79**, 155107 (2009)
- [57]. A. Tkatchenko, M. Scheffler, *Phys. Rev Lett.* **102**, 073005 (2009)

## APPENDIX

A1. Convergence

A2. Energy calculation sample files

1. INCAR file

MnSe

NPAR = 8

NELM = 250

ISIF = 3

NSW=60

IBRION = 2

POTIM = 0.2

ISMEAR = 1

SIGMA = 0.2

ISPIN = 2

MAGMOM = 2 -2 0 0

GGA = BO

PARAM1 = 0.1833333333

PARAM2 = 0.2200000000

LUSE\_VDW = .TRUE.

AGGAC = 0.0000

ENCUT = 500

EDIFF = 1E-6

EDIFFG = -0.005

## 2. Kpoints file

A

0

M

19 19 1

## 3. POSCAR file

MnSe

1.0000000000000000

3.9979284476539445 0.0000000000000000 0.0000000000000000

0.0000000000000000 3.9979284476539445 0.0000000000000000

0.0000000000000000 0.0000000000000000 18.0000000000000000

Mn Se

2 2

Direct

-0.0000000000000000 0.0000000000000000 0.0000000000000000

0.5000000000000000 0.5000000000000000 0.0000000000000000

0.0000000000000000 0.5000000000000000 0.9183271448904622

0.5000000000000000 -0.0000000000000000 0.0816728551095378

0.00000000E+00 0.00000000E+00 0.00000000E+00

0.00000000E+00 0.00000000E+00 0.00000000E+00

0.00000000E+00 0.00000000E+00 0.00000000E+00

0.00000000E+00 0.00000000E+00 0.00000000E+00

Formation energy of inverted-litharge MnSe

$$E_f = E_{2D}/N_{2D} - E_{\text{bulk}}/N_{\text{bulk}}$$

$$= -4.551 - (-4.547) \text{ meV/atom}$$

$$= 23 \text{ meV/atom}$$

### A3. Phonon calculation

#### Step 1

INCAR file

FeSe

ISIF = 3

NSW=60

IBRION = 2

POTIM = 0.2

ISMEAR = 1

SIGMA = 0.05

ISPIN = 1

ENCUT = 500

EDIFF = 1E-7

EDIFFG = -0.005

NELM = 250

#### 2. KPOINTS file

A

0

M

20 20 1

#### 3. POS CAR file

FeSe

1.0000000000000000

3.6666213951773736 0.0000000000000000 0.0000000000000000

0.0000000000000000 3.6666213951773736 0.0000000000000000

0.0000000000000000 0.0000000000000000 18.0000000000000000

Fe Se

2 2

Direct

-0.0000000000000000 0.0000000000000000 0.0000000000000000

0.5000000000000000 0.5000000000000000 0.0000000000000000

0.0000000000000000 0.5000000000000000 0.9220777533582125

0.5000000000000000 0.0000000000000000 0.0779222466417875

0.00000000E+00 0.00000000E+00 0.00000000E+00

0.00000000E+00 0.00000000E+00 0.00000000E+00

0.00000000E+00 0.00000000E+00 0.00000000E+00

0.00000000E+00 0.00000000E+00 0.00000000E+00

Step 2

Creating a supercell

phonopy -d --dim="4 4 1" -c POSCAR-unitcell

mv SPOSCAR POSCAR

1. INCAR file

FeSe

PREC = Accurate

ISIF = 2

NSW=1

NELM = 250

IBRION = 8

IALGO = 38

ISMEAR = 1

SIGMA = 0.05

ENCUT = 500

EDIFF = 1E-7

ADDGRID = .TRUE.

LWAVE = .FALSE.

LCHARGE = .FALSE.

LREAL = .FALSE.

Change KPOINTS to 5 5 1.

phonopy --fc vasprun.xml

phonopy --dim="2 2 2" -c POSCAR-unitcell band.conf

Then we could plot the phonon spectrum.

#### A4. Band structure HSE functional

Step 1.

SYSTEM = FeS

ISTART = 0; ICHARG = 2

ENCUT = 500

ISMEAR = 0; SIGMA = 0.01

IBRION = 2

ISIF = 3

POTIM = 0.2

EDIFF = 1E-6

GGA = PE

ISPIN = 1

PREC = Accurate

Step 2.

SYSTEM = FeS

ISTART = 1; ICHARG = 2

ENCUT = 500

ISMEAR = 0; SIGMA = 0.01

EDIFF = 1E-5

NELM = 250

GGA = PE

ISPIN = 1

PREC = Accurate

LHFCALC = .TRUE.

HFSCREEN = 0.2

PRECFOCK = N

ALGO = ALL

TIME = 0.4

LWAVE = .TRUE.

LCHARG = .TRUE.

LVTOT = .TRUE.

LORBIT = 11